Effects of cohesion and viscosity on lava dome growth following repose

Amy Myers, Claire Harnett, Eoghan Holohan, John Ryan, Edgar Zorn,
Thomas Walter, Michael Heap

To cite this version:

Amy Myers, Claire Harnett, Eoghan Holohan, John Ryan, Edgar Zorn, et al.. Effects of cohesion and viscosity on lava dome growth following repose. Journal of Volcanology and Geothermal Research, 2024, 455, pp.108196. 10.1016/j.jvolgeores.2024.108196 . hal-04743982

HAL Id: hal-04743982
https://hal.science/hal-04743982v1

Submitted on 19 Oct 2024

Journal of Volcanology and Geothermal Research 455 (2024) 108196

Contents lists available at ScienceDirect

Journal of Volcanology and Geothermal Research

journal homepage: www.journals.elsevier.com/journal-of-volcanology-and-geothermal-research

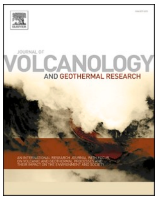

Effects of cohesion and viscosity on lava dome growth following repose

Amy J. Myers[a,*], Claire E. Harnett[a,*], Eoghan P. Holohan[a], John G. Ryan[b], Edgar U. Zorn[c], Thomas R. Walter[d], Michael J. Heap[e,f]

[a] *UCD School of Earth Sciences, University College Dublin, Belfield, Dublin, Ireland*
[b] *UCD School of Civil Engineering, University College Dublin, Belfield, Dublin, Ireland*
[c] *Earth and Environmental Sciences, Ludwig Maximilian University of Munich, Theresienstr. 41, Munich, Germany*
[d] *GFZ German Research Centre for Geosciences, Telegrafenberg, 14473 Potsdam, Germany*
[e] *Université de Strasbourg, CNRS, Institut Terre et Environnement de Strasbourg, UMR 7063, 5 Rue Descartes, Strasbourg F-67084, France*
[f] *Institut Universitaire de France (IUF), Paris, France*

ARTICLE INFO

Keywords:
Lava dome
Lava spine
Analogue modelling
Scaling
Viscous
Digital image correlation

ABSTRACT

Lava domes result from effusive eruption of high viscosity lava. These viscous lava extrusions range in shape from flat-topped domes with small height-to-width aspect ratios, to spine-like columns exhibiting large height-to-width aspect ratios. A primary control on morphology during early dome growth is thought to be the variation in rheological characteristics of extruded material. In this work, we present new scaled analogue models of lava dome growth that consider extrusion of a frictional plastic upper-conduit plug followed by viscous magma. We simulate the brittle plug using a sand-plaster mixture, the cohesion of which is varied by plaster content. We model the magma using sugar syrup, the viscosity of which is controlled by the weight percent of added crystalline sugar. The models both qualitatively and quantitatively reproduce part of the spectrum of natural dome morphology not previously obtained in most past analogue modelling studies. Model aspect ratios of 0.02 to 0.9 capture approximately 90 % of the reported aspect ratio variation in nature. Increasing plug cohesion results in extrusions with higher aspect ratios and spinier morphologies. Low viscosity fluid typically erupts through the brittle dome, whilst high viscosity fluid tends to promote endogenous growth or emerge as exogenous lobes. Particle Image Velocimetry shows that fracture localisation at the dome surface is cohesion-dependent, and eruption of fluid follows shear fractures within the dome. Where fluid remains contained within the dome, we see lateral spread leading to a wider and flatter dome morphology. Evolution of lava dome morphology, deformation, and associated hazards is guided by the complex rheological properties of the extruded material; we suggest that during episodic dome growth, these properties are largely defined in the conduit prior to their eruption.

1. Introduction

Lava domes form from the extrusion of highly viscous magma and are common features at andesitic or dacitic stratovolcanoes (Fig. 1). Lava domes can collapse through gravitational instability, such that rapid decompression and surface exposure of the hot dome core can result in explosions (Harnett et al., 2019; Voight and Elsworth, 2000). Collapse events can generate deadly pyroclastic flows, such as those that devastated half of the island of Montserrat, Eastern Caribbean (Calder et al., 2002; Cole et al., 1998) or the collapse that killed 43 people at Mount Unzen in 1992 (Nakada et al., 1999). As a result, there has long been volcanological interest in understanding the evolution of lava dome geometry, structure, and stability.

Eruption of high viscosity lava can form thick, stubby flows, coulees, and domes (Harris and Rowland, 2015; Calder et al., 2015). The morphology of these emplaced structures is primarily governed by viscosity, magma porosity and crystallinity, eruption rates, cooling rates, and local topographic features (see Myers et al., 2024 and references therein). We focus here on lava domes, observations of which in nature have revealed a geometric spectrum ranging from flat-topped domes through to large, monolith-like spines (Fig. 1). This geometric spectrum can be quantitatively and qualitatively described by considering factors such as dome height, width, aspect ratio, volume, and surface features and structures (e.g., fractures, crease structures, compressional ridges, block distribution; see also Fink and Anderson, 2000). In this study, we focus on simple quantitative measures of dome growth: height (H),

---

* Corresponding authors.
E-mail addresses: myers.amyj@outlook.com (A.J. Myers), claire.harnett@ucd.ie (C.E. Harnett).

https://doi.org/10.1016/j.jvolgeores.2024.108196
Received 22 July 2024; Received in revised form 19 September 2024; Accepted 27 September 2024

width (W), and aspect ratio (AR) which is defined in this study as H/W (e.g., Myers et al., 2024; Ogburn et al., 2012-). The range of observed dome geometries spans aspect ratios from <0.1 (low lava domes, e.g., Závada et al., 2015; flat-topped domes, e.g., Watts et al., 2002) to >3.0 (spines; Lacroix, 1904).

Current conceptual models of active lava dome structure (Fig. 2) suggest the presence of (i) an inner, hot, ductile or fluid core, (ii) an enclosing carapace of variable thickness through time, and (iii) an outer, mechanically detached talus region formed from broken brittle material (Harnett and Heap, 2021; Iverson, 1990; Wadge et al., 2009). Viscosity of the fluid core, i.e., its resistance to flow once at the surface, is dependent on several inter-related factors including crystallinity, volatile content, and temperature. Crystallinity and volatile content are influenced by magma residence time in the upper conduit (e.g., Cassidy et al., 2015; Melnik and Sparks, 2005; Smith et al., 2011; Sparks et al., 2000). The cohesive strength of the solid crust, which relates to the material's ability to withstand tensional stress, is typically controlled by degassing, vesicle proportion, and crystallisation (e.g., Heap et al., 2016). Cohesive strength of the outer shell has been shown to influence dome geometry by increasing the resistance to lateral flow through confinement of the enclosed dome core and therefore facilitating growth of higher AR features (Husain et al., 2018; Zorn et al., 2020).

Previous studies have suggested that the spreading of a dome, and therefore its morphology, depends primarily on the mechanical strength of the solid carapace (e.g., Iverson, 1990; Buisson and Merle, 2005). An alternative is that that dome shape (i.e., ratio of height to width) is controlled by the *combined* influence of the viscosity and strength of the core, outer crust, and surrounding talus apron (Swanson and Holcomb, 1990). For example, steep Pelean domes are dominantly controlled by internal friction of the surrounding talus pile, while low lava domes are dominantly controlled by the yield strength of the spreading fluid core (Blake, 1990). A series of studies in the 1990s (e.g., Fink and Bridges, 1995; Griffiths and Fink, 1997; Fink and Griffiths, 1998) showed that the key variable controlling dome morphology is the ratio of cooling rate to extrusion rate (see also Section 4.2), as this controls the thickness of the crust and therefore determines whether solidification plays a dominant role in growth.

Domes can grow continuously, where lava extrusion occurs at a near-constant extrusion rate until the dome becomes gravitationally unstable and collapses. Alternatively, domes grow episodically, with bouts of extrusion separated by periods of repose. Episodic growth typically allows for a higher degree of cooling relative to extrusion rate. Dome growth episodes can be separated by repose periods on the timescale of days (e.g., Mount St. Helens, USA, Swanson and Holcomb, 1990) to years (e.g., Soufrière Hills Volcano, Montserrat, Sparks and Young, 2002; Wadge et al., 2014). In the case of cyclic dome growth, with paused and then renewed eruption, magma within the shallow conduit commonly undergoes prolonged degassing and/or crystallisation. Prior to lava eruption, a solidified magma cap or plug can thereby form toward the top of the conduit and overlie a viscous zone of semi- to fully molten material deeper in the conduit (Iverson, 2008). For example, time-lapse imagery and numerical modelling of the 2013 dome at Volcán de Colima, Mexico, showed that the initial rapid increase in dome height could be explained by extrusion of an initially stronger material or cohesive plug (Walter et al., 2019). Photographs of the dome showed that a high aspect ratio (AR = 2.1) spine-like feature appeared at the start of extrusion, but this transitioned to a lower aspect ratio (AR = 0.6) dome once lateral spreading dominated growth.

Given the hazardous nature of collecting data in the field, analogue and numerical models have been used to study the processes influencing lava dome growth and morphology. Numerical models are best employed to investigate the underlying physics acting in a system and provide the opportunity to investigate lava dome growth at full scale (e.g., Hale, 2008; Harnett et al., 2018; Husain et al., 2019; Tsepelev et al., 2020; Zeinalova et al., 2021). The complex rheological variation and high strain deformation characteristic of lava dome growth, however, renders them difficult to simulate in numerical models in three dimensions. Analogue models overcome such limitations by using a scaled down representation of the physical system with materials of suitable rheological properties (e.g., Blake, 1990; Griffiths and Fink, 1997; Zorn et al., 2020).

Analogue modelling studies of lava dome growth have to date used a

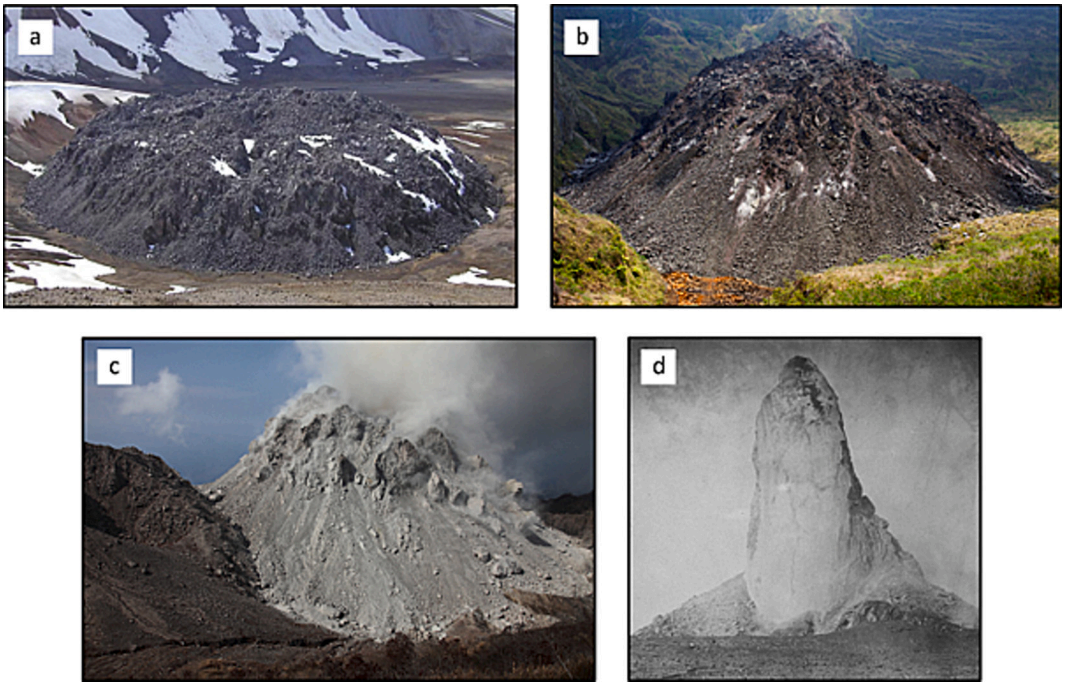

Fig. 1. Photographs showing part of the spectrum of geometries of lava domes and lava spines found in nature: **(a)** Novarupta, Alaskan Peninsula Volcanic Arc, USA (AR = 0.18; photo by USGS); **(b)** Kelud, Sunda Volcanic Arc, Indonesia (AR = 0.42; photo by Øystein Lund Andersen); **(c)** Paluweh, Sunda Volcanic Arc, Indonesia (AR = 0.67; photo by Richard Roscoe); **(d)** Pelée, Lesser Antilles Volcanic Arc, France (AR = 3.0; photo from the USGS).

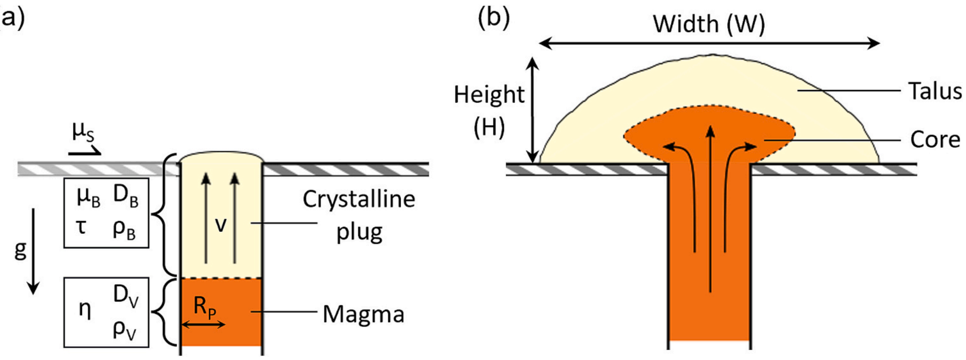

Fig. 2. Conceptual cross section of lava dome growth. (a) onset of plug extrusion; (b) continued extrusion after plug collapse with formation of talus around a molten dome core. We show the parameters that we identified as key to this study in (a), and the measured result parameters in (b). Pre-extrusion brittle material parameters: depth (D_B); density (ρ_B); friction coefficient (μ_B); cohesion (τ). Pre-extrusion viscous material parameters: depth (D_V); density (ρ_V); viscosity (η). System parameters: substrate friction coefficient (μ_S); acceleration due to gravity (g); pipe radius (R_P); ascent velocity (v).

single dome-forming material. Most studies have used a viscous fluid such as silicone polymer (e.g., Fink and Bridges, 1995), water-clay slurries (e.g., Blake, 1990), and wax-clay mixtures (e.g., Fink and Griffiths, 1998). These studies mostly replicated the geometries of axisymmetric, low-AR extrusions. For example, Blake's analogue domes (Blake, 1990) using a water-clay slurry produced domes with AR between 0.10 and 0.35. Typical aspect ratios found by Fink and Bridges (1995) were < 0.33, with higher aspect ratios (0.59, 0.80) produced by thermal conditions and flux rates that induced rapid solidification of the temperature-dependent liquid polyethylene glycol (PEG; Fink and Griffiths, 1990). A recent study (Zorn et al., 2020) used a granular material comprising either silica sand or a mixture of sand and gypsum (plaster). Models with sand only produced aspect ratios of 0.23, whilst mixtures of sand with 30 wt% plaster were able to reproduce higher aspect ratios up to 1.55, a result compatible with extrusion of strong (more cohesive) near-solid lava during spine-forming growth phases (Zorn et al., 2020).

Here we present results from new scaled analogue experiments of lava dome growth conducted with both a viscous fluid and a granular material. This specifically aims to investigate the hypothesis that dome growth is mechanically controlled by the interplay between the 'strengths' of the viscous core and brittle solid. In particular, we simulate renewed dome growth after a pause in extrusion, whereby a plug of stiffer magma has formed in the shallow conduit and is extruded first, followed by fresher viscous magma (Fig. 2). Our goal is to more fully capture, and thus better understand, the rheological controls on lava dome morphology and its structural evolution during early dome growth.

2. Methods

We performed analogue modelling to investigate the effects of both viscosity and cohesion on lava dome morphology. To better replicate the contrasting material behaviours of the different components of lava domes in nature, we conducted experiments using a sugar-syrup suspension as a viscous fluid analogue and mixtures of sand plus gypsum plaster as a granular solid analogue. In nature, the proportions of fluid and solid components likely change through time, as reducing magma flux promotes increased cooling and consequent growth of the carapace and talus relative to the core (Wadge et al., 2009). As they do not explicitly incorporate such thermal effects, our models are best matched to the early stages of lava dome growth dominated by crystalline plug extrusion (see all Section 4.2) after a period of repose. We measure height, width, and aspect ratio of the growing domes through time, as well as using Particle Image Velocimetry (PIV) to analyse deformation patterns.

2.1. Experimental rig

The experimental rig is designed to enable material to be pushed out of the top of a pipe (conduit) by a piston head, which is driven upwards by a motor (Fig. 3). A table topped with a removable board that has a 400 mm × 400 mm grid of 10 mm × 10 mm laser-cut squares forms the extrusion surface. We quantified the frictional properties of the extrusion surface using a simple block pull method (see **Supplementary Material S1**) and found a friction coefficient of 0.4 (friction angle of ~22°). A stainless-steel pipe (38.1 mm internal diameter, 300 mm total functional length) is fixed in place below the table such that the upper end sits flush with the extrusion surface. The piston head is made of self-lubricating plastic and is attached to a rack; use of a rack-and-pinion system eliminates any rotational component to the piston motion and thus any related torsional stress. Material loss through the space between the piston head and the internal wall of the pipe is minimised by capping the piston head with a 1 mm-thick neoprene disc. The rack-and-pinion system is connected to a P Series Nema 34 Bipolar stepper motor controlled by an Arduino Uno open-source microcontroller board via a DM860T digital stepper driver operating at 20,000 steps/revolution and with a peak current of 7.2 A. Using this arrangement, we can specify a piston head travel distance and rate of ascent. To achieve the low ascent rates needed to replicate natural systems, the motor is also connected to an EG Series Planetary Gearbox with a 50:1 gear ratio. In all experiments presented here, we use a constant ascent rate of 1.5 mm/min with an experiment duration of 100 min.

To facilitate data collection, an array of three cameras, two horizontal and one aerial, took timelapse photographs every minute during the experiment; models and configurations are listed in Table 2. Before loading the conduit with granular material, the cameras are focused and calibrated with the open-source software DigiCamControl v.2.1.6. Calibration is required to ensure the focal depth matches the cross-section of the conduit so that our images are in focus throughout the dome growth. The cameras remain in manual focus mode to ensure the focal length, and therefore calibrated scale, is constant throughout the series of images.

2.2. Analogue materials

Much literature exists on the behaviour, properties, and suitability of common analogue materials for modelling various aspects of volcanic systems (see Kavanagh et al. (2018) for a comprehensive overview). Guided by the material characterisation studies of Castruccio et al. (2010) and Poppe et al. (2021), by the experiment results of Zorn et al. (2020), and by our own dimensional scaling analysis (Section 2.4 below), we used a sand-gypsum mixture as the granular solid and a syrup-sugar suspension as the viscous fluid.

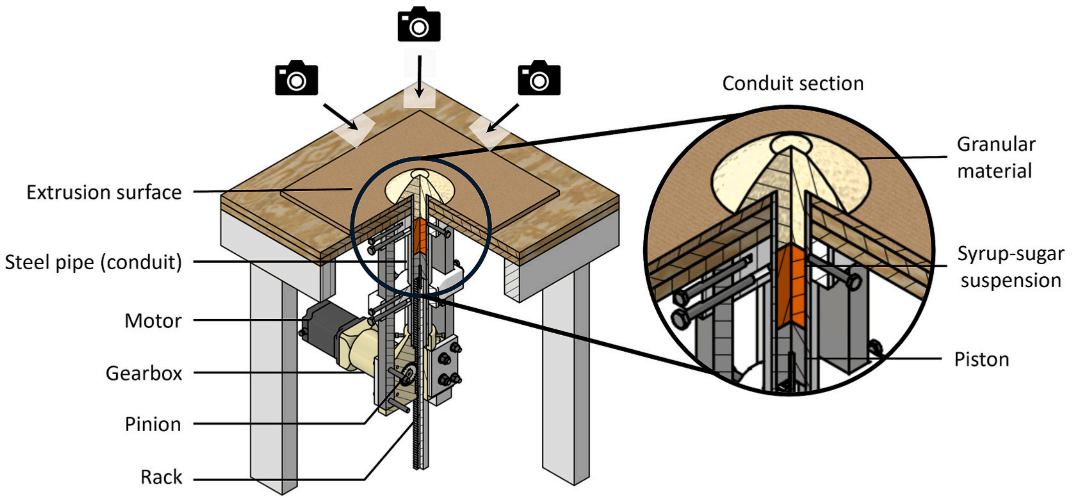

Fig. 3. Technical drawing of the design of the rig, showing the arrangement of key components. The structure of material in the conduit is illustrated in the zoomed in portion. Conduit diameter is 38.1 mm.

2.2.1. *Sand and gypsum plaster*

To produce the granular solid mixture, we added gypsum plaster to a sand base. Samples of the sand and plaster were observed using a LEICA ES2 Microscope at 30× magnification with a reflected light source. In the sand, sub-rounded to rounded quartz grains were dominant (~95 %). The remaining ~5 % of grains were rounded plagioclase and orthoclase feldspars, and subangular amphiboles and pyroxenes. The grains were well-sorted with sizes ranging from 150 μm (fine sand) to 420 μm (medium sand) based on measurements from 30 randomly selected grains. The plaster had grain sizes that were too small to be determined using an optical microscope; grain size analysis conducted by Poppe et al. (2021) for the same material gave an average grain size of 22 μm.

As the mechanical properties of gypsum are affected by moisture (Poppe et al., 2021), we first dried the plaster in an oven at 80 °C for 18 h before storing it in a sealed container. The gypsum and sand were then mixed immediately prior to (c. 10 mins before) each experiment run. The ambient air humidity was maintained at 35–45 % for all experiments.

The proportion of gypsum plaster in the sand controls the cohesion of the granular material, whereby a higher plaster content is associated with higher cohesion (τ) and higher tensile strength (Poppe et al., 2021). In our experiments, we used three sand-plaster mixtures with plaster proportions of 0 wt%, 10 wt%, and 20 wt%. Based on laboratory characterisation performed by Poppe et al. (2021), we estimate that these materials have a cohesion of <200 Pa, < 250 Pa, and < 300 Pa, respectively, and a friction coefficient (μ_B) of 0.7–0.8.

2.2.2. *Sugar syrup and crystalline sugar*

We used a suspension of added crystalline sugar in invert sugar syrup (specifically using Gem Golden Syrup) as the magma analogue. We used a bimodal size distribution dominated by fine crystals at a ratio of 10:1, with icing sugar as the fine fraction (mean grain size 50–75 μm) and granulated sugar as the coarse fraction (mean grain size 450–600 μm). The sugar proportion is given as a weight percent of the total suspension mass. We use two sugar crystal sizes following previous studies that showed a strong dependence of syrup suspension viscosity on bimodal crystal size (Castruccio et al., 2010). The syrup and sugar were mixed by hand until the suspension had a smooth and even texture with no lumps of sugar. We prepared the suspension immediately prior to setting up and conducting the experiment to minimise settling of the suspended particles and avoid any possible wetting of the sand-plaster mix.

We carried out viscometry of four syrup-sugar suspensions (0 wt%, 10 wt%, 30 wt%, and 50 wt%) by using a Brookfield DV3T Rotational Rheometer at room temperature (Fig. 4). Increasing the proportion of sugar crystals in the suspension resulted in a mixture with a higher dynamic (absolute) viscosity (η). At mid-range shear rates, of 0.13 s^{-1} (equivalent to 1 RPM), $\eta_0 = 32$ Pa•s (0 wt% sugar), $\eta_{10} = 106$ Pa•s (10 wt% sugar), $\eta_{30} = 227$ Pa•s (30 wt% sugar), and $\eta_{50} = 1264$ Pa•s (50 wt % sugar). In addition, the sugar-syrup suspensions exhibited increasingly non-Newtonian behaviour as the concentration of sugar crystals increased, i.e., as shear rate increased from 0.03 s^{-1} to 0.24 s^{-1}, the measured viscosity decreased by an amount that was progressively greater with increased sugar concentration (Table 1). Such shear thinning behaviour observed in the high-sugar suspensions replicates the characteristics of crystal-bearing magmas (e.g., Lavallée et al., 2007). The shear rate in our experiments is 0.0013. We therefore estimate the viscosity in the experiments by extrapolating our measured viscosities using a fitted curve (equations for which can be found in the caption for Fig. 4).

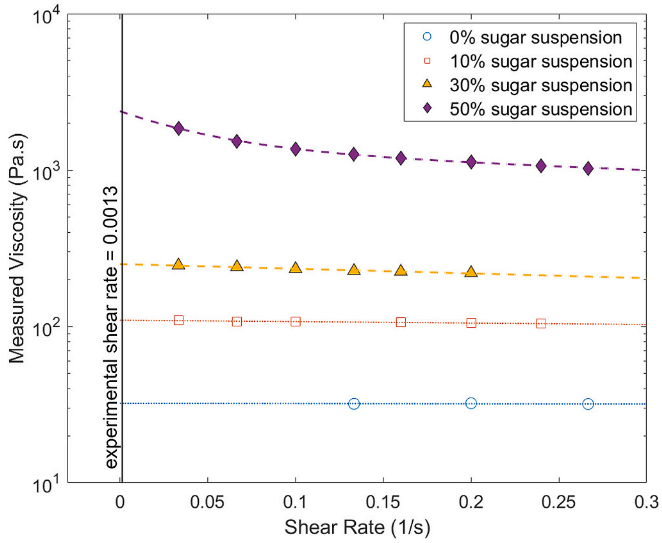

Fig. 4. Graph of syrup mixture viscosity as a function of crystalline sugar content for a range of shear rates. Suspensions with 30 wt% and 50 wt% sugar (filled symbols) are used in our experiments as the low and high viscosity fluids, respectively. The solid vertical line denotes the shear rate (0.0013) associated with a piston ascent rate of 1.5 mm/min. Equations for each line are: $\eta_0 = -1.13\dot{\gamma} + 32.25$; $\eta_{10} = -22.33\dot{\gamma} + 109.6$; $\eta_{30} = 250.6e^{-0.69\dot{\gamma}}$; and$\eta_{50} = 1049e^{-18.98\dot{\gamma}} + 1332e^{-0.97\dot{\gamma}}$.

Table 1

Measured viscosities (η) of four syrup-sugar suspensions at shear rates of 0.03 s^{-1} and 0.24 s^{-1}, and the calculated viscosity difference (Δη). Negative Δη values signify decreasing viscosity with increasing shear rate i.e., shear-thinning non-Newtonian behaviour.

Suspension (sugar wt%)	$\eta_{0.03}$ (Pa•s)	$\eta_{0.24}$ (Pa•s)	$\Delta\eta = \eta_{0.24} - \eta_{0.03}$ (Pa•s)	$\eta_{0.0013}$ (experimental) (Pa•s)
0	32	32	0	32
10	109	104	−5	110
30	246	212	−34	250
50	1851	1063	−788	2354

Table 2

Summary of hardware configurations used to capture time-lapse images throughout the experiments.

Camera and Lens	Viewing Angle	Focal Length	Distance from Focal Point
Nikon D5300 DSLR with 18–55 mm kit lens	Profile 1	24 mm	300 mm
	Profile 2	32 mm	350 mm
	Overhead	55 mm	600 mm

Based on our scaling considerations (Section 2.4), we selected the 30 wt% sugar-syrup suspension as our “low viscosity” endmember and the 50 wt% sugar-syrup suspension as our “high viscosity” endmember. Extrapolation of the viscometry data to the shear rate of 0.0013 imposed in each experiment (Fig. 4) yields estimated dynamic viscosities of 2354 Pa.s and 250 Pa.s for 50 wt% and 30 wt% gypsum, respectively.

2.2.3. *Material handling*

In experiments with only granular material, we fill the conduit to a depth of 150 mm with sand-plaster mix. In experiments with both granular material and viscous fluid, we fill the lower 45 mm (30 %) of the conduit with viscous fluid and the remaining 105 mm (70 %) with granular material (see Fig. 3). We chose these quantities based on natural spine observations; we estimate the Pelée spine was ~315 m in height, suggesting that the conduit plug reached this depth before extrusion. In our scaled model, 1 mm approximately represents 3 m in nature, so we use a “plug” depth of 105 mm (i.e., 315 m).

We load the viscous fluid into the steel pipe conduit via a length of PVC pipe as this ensures that we deliver the fluid directly to the bottom of the conduit. This method avoids the contamination of the conduit walls with fluid, which could alter the observed behaviour of the overlying granular material. The final preparatory step is adding the well-mixed granular material to the conduit using a funnel. This is left until last to minimise the length of time the two materials are in contact with each other, otherwise there is the potential to develop an interface of stiffer material at the base of the granular material.

2.3. *Image analysis*

Here, we give full details for the image analysis performed to provide first-order quantitative observations of height (H), width (W), and aspect ratio (H/W) to facilitate future replication of our experiments. For each experiment, we measured the maximum height and width of the extrusion at intervals of one minute. We segmented the time-lapse photographs in MATLAB® using the Color Thresholder app. This technique isolates a region of interest by restricting the ranges of three channels that define a colour space, thus producing a binary image. Filtering in the HSV space (hue, saturation, and value) consistently produced the most accurate binary image. The function obtained by segmenting one image is then used to automatically segment all other images within an experiment and dimensions are automatically extracted.

For the profile images, we defined the extrusion base as the row number at the midpoint of the line between the first and last pixel (from left to right) contained in the region of interest. Dimensions could then be calculated and converted from pixels to centimetres using a conversion factor determined from a scaled image taken before each experiment. Average height was calculated from two values, one from each profile image. Width was calculated by fitting a bounding box to segmented aerial images and taking an average of the major and minor diameters.

We also applied PIV to track surface deformation and fracture formation between image frames. For this, pixel movements were vectorised using the software DaVIS (Version 10.0.5) from LaVision and by undertaking a multi-pass cross correlation with an initial search window size of 96 px at 50 % overlap, followed by a search window size of 32 px at 75 % overlap. Pixel displacements were converted to lengths using the scaled image acquired before each experiment. This procedure generates surface displacement vectors that highlight the magnitude and direction of motion in the image plane and that allow for the calculation of normal strain to highlight areas of significant differential motion (i.e. opening fractures).

2.4. *Scaling analysis*

We scaled the experiments using dimensional analysis; this is a well-established approach that ensures geometric, kinematic, and dynamic similarity between natural systems and models (e.g., Barenblatt, 2003; Fink and Griffiths, 1990; Galland et al., 2018; Holohan et al., 2023; Hubbert, 1937; Merle, 2015).

The scaling procedure consists of four key steps:

1. Identifying governing parameters and output parameters (see Fig. 2a for a labelled schematic of the experimental rig). A governing parameter is any variable that influences the form of the output in an experiment.
2. Obtaining dimension functions for each governing parameter. A dimension function expresses a variable in terms of a class of units. We used the LMT system which has units for length, mass, and time, respectively. **Supplementary Material S2** lists the governing parameters and their respective dimension functions
3. Assessing each parameter as dependent or independent. A dimension function is independent if it cannot be expressed as a product of other independent dimension functions raised to any power (Barenblatt, 2003).
4. Defining the relevant Π numbers. Each Π number is dimensionless and therefore represented as a geometric or kinematic ratio, the exact formulation of which is guided by existing insights into the system.

Full similarity is achieved when the values of the Π numbers are approximately equal (similar order of magnitude) for both the experimental and natural systems. The values of the Π numbers for the models and nature are summarised in Fig. 5 below.

3. Results

We systematically explored the effect of cohesion and viscosity by carrying out experiments using (1) only granular material (sand, sand with 10 wt% gypsum, and sand with 20 wt% gypsum); (2) each granular material with a low viscosity syrup-sugar suspension, with 30 wt% sugar; and (3) each granular material with a high viscosity syrup-sugar suspension, with 50 wt% sugar. Full gifs of all experiments are provided in the **Supplementary Material S3**, with images captured each minute from the three cameras shown in Section 2.1. In addition, we provide all raw images online at Zenodo: https://doi.org/10.5281/zenodo.13749011 and tables of all H, W, and AR in an Excel spreadsheet in **Supplementary Material S4**. Throughout this section we provide quantitative descriptions of the results to accompany the figures. We do

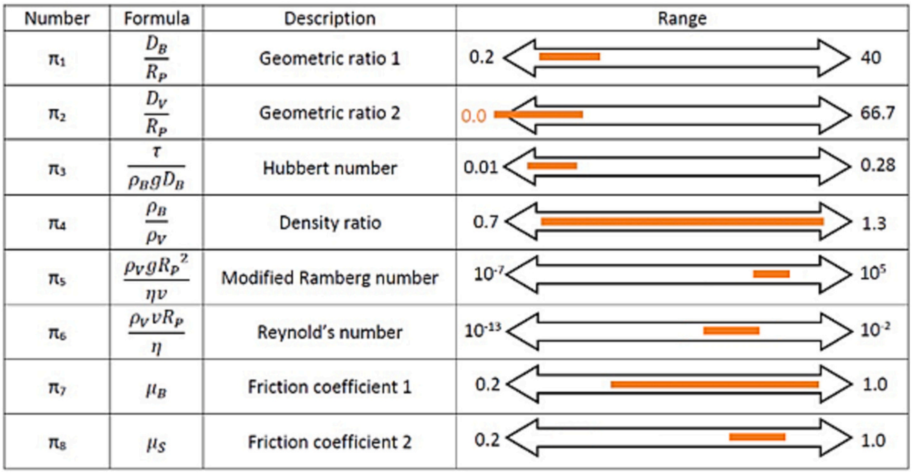

Number	Formula	Description	Range	
π_1	$\frac{D_B}{R_P}$	Geometric ratio 1	0.2	40
π_2	$\frac{D_V}{R_P}$	Geometric ratio 2	0.0	66.7
π_3	$\frac{\tau}{\rho_B g D_B}$	Hubbert number	0.01	0.28
π_4	$\frac{\rho_B}{\rho_V}$	Density ratio	0.7	1.3
π_5	$\frac{\rho_V g {R_P}^2}{\eta v}$	Modified Ramberg number	10^{-7}	10^5
π_6	$\frac{\rho_V v R_P}{\eta}$	Reynold's number	10^{-13}	10^{-2}
π_7	μ_B	Friction coefficient 1	0.2	1.0
π_8	μ_S	Friction coefficient 2	0.2	1.0

Fig. 5. Equations and descriptions for the eight dimensionless Π numbers used in the scaling analysis. The final column shows the expected range for each number in nature (black arrows) and calculated ranges for the models (orange bars).

this to allow quantitative comparison between our experiments, rather than to infer quantitative comparisons with nature. The automated dimensions provided here relate to the maximum height and width of the whole dome complex; this approach is further discussed in Section 4.1.

3.1. *Granular material only*

The first suite of experiments used only granular material. We extruded a 150 mm long column of sand with (a) 0 wt% gypsum; (b) 10 wt% gypsum; and (c) 20 wt% gypsum, onto the extrusion surface. These are similar to the experiments carried out by Zorn et al. (2020), and we present them here for full comparison with the models that include a viscous fluid.

3.1.1. *Sand only*

Extrusion of only sand produced an axisymmetric flat-topped dome with sides sloped at ~30° (Fig. 6a). The first 20 min of extrusion (30 mm of piston displacement) were accompanied by a rapid increase in aspect ratio from ~0.05 to ~0.3 (Fig. 6d), producing a dome with H = 20 mm and W = 66 mm. The dome continued to grow laterally by way of small avalanches and maintained a dome aspect ratio of 0.25–0.3 and a lateral slope angle of 30° throughout the remainder of the experiment (~ 80 min). We observed no obvious pattern or order to the origin locations of the avalanches in plan view. The final dome was circular when viewed from above, had a flat top, and final dimensions of H = 32 mm, W = 126 mm, and AR = 0.25.

3.1.2. *Sand plus 10 wt% gypsum mixture*

Extrusion of sand with a low gypsum content produced transient spiny protrusions from the dome top (Fig. 6b). Visually, early extrusion differed from sand-only extrusion, as with a sand-gypsum mix we initially observed a more cohesive central column. The column top contained a set of polygonal blocks due to fracturing in its upper few millimetres. The column rapidly disintegrated, however, such that the aspect ratio evolution in the first 20 min of extrusion mirrored that in the pure sand experiment (Fig. 6d). After 20 min (30 mm of piston displacement), growth transitioned to cycles of small-scale spine protrusion and collapse. Spines rose through the centre of the dome to approximately 5–10 mm above the upper dome surface. The spines had prismatic 3D geometries and widths of ~10 mm. The spines reached a maximum height of ~10 mm above the dome surface before collapsing, with the rapid addition of the collapsed material to the upper surface of the dome triggering avalanching. We observed six full cycles of spine generation and collapse as identified in the sawtooth pattern of the aspect ratio curve in Fig. 6d. Compared to the sand-only extrusion, the overall dome geometry was closer to conical and had steeper lateral slope angles of around 40°. After 100 min, the dome-spine complex had final dimensions of H = 47 mm, W = 130 mm, and AR = 0.35.

3.1.3. *Sand plus 20 wt% gypsum mixture*

Extrusion of sand with a high gypsum content produced larger and longer-lived spine protrusions that dominated the extrusion form (Fig. 6c). We first observed a central column with a diameter equal to the conduit diameter that reached an aspect ratio of ~0.45 (height of 50 mm) before partial collapse (Fig. 6d). We again observed cycles of spine growth and collapse, but with fewer cycles, longer cycle lengths (15–30 min), and maximum dome-spine complex aspect ratios of ~0.7 prior to collapse. Spine collapse was rapid and led to significant and sudden decreases in dome height. For each collapse, we observed corresponding increases in dome width as the collapsed material formed part of the talus. These larger spine collapses with higher plaster content are evidenced by the sharper decreases in AR seen in Fig. 6d. Furthermore, the AR of the dome-spine complex immediately following each of the collapses (0.30–0.40) was consistently higher than we observed in the low gypsum case (0.25–0.30). Because of the dominance of the spines, slope angles commonly exceeded 45°. After 100 min, the dimensions of the dome-spine complex were H = 65 mm, W = 151 mm, and AR = 0.43.

3.2. *Granular material with a low viscosity fluid*

The next suite of experiments used a two-material conduit. The bottom 45 mm of the conduit contained a low viscosity syrup-sugar suspension with 30 wt% sugar crystals. The remaining 105 mm of the conduit was filled with a granular mixture of sand and (a) 0 wt% gypsum; (b) 10 wt% gypsum; and (c) 20 wt% gypsum.

3.2.1. *Sand with low viscosity fluid*

Extrusion of a two-material column produced an axisymmetric dome of granular material from which a lobate fluid flow originated (Fig. 7a). In the first 20 min of extrusion, the dome reached H = 20 mm and W = 73 mm. As in the no-fluid experiment with sand only, the dome grew laterally by way of small avalanches and maintained a near constant aspect ratio of 0.25–0.29 throughout the remainder of the experiment. At $T = 70$ min (vertical dashed line in Fig. 7d), the granular portion of the column had been extruded and the fluid portion began intruding into the established dome, which had grown to H = 29 mm and W = 114 mm. At $T = 84$ min, the fluid broke through the granular material (Fig. 7a); this was also when the dome reached its maximum height of 35 mm. During the final 16 min of the experiment, fluid continued to extrude from the dome to form a lobate flow around the dome base. The dome

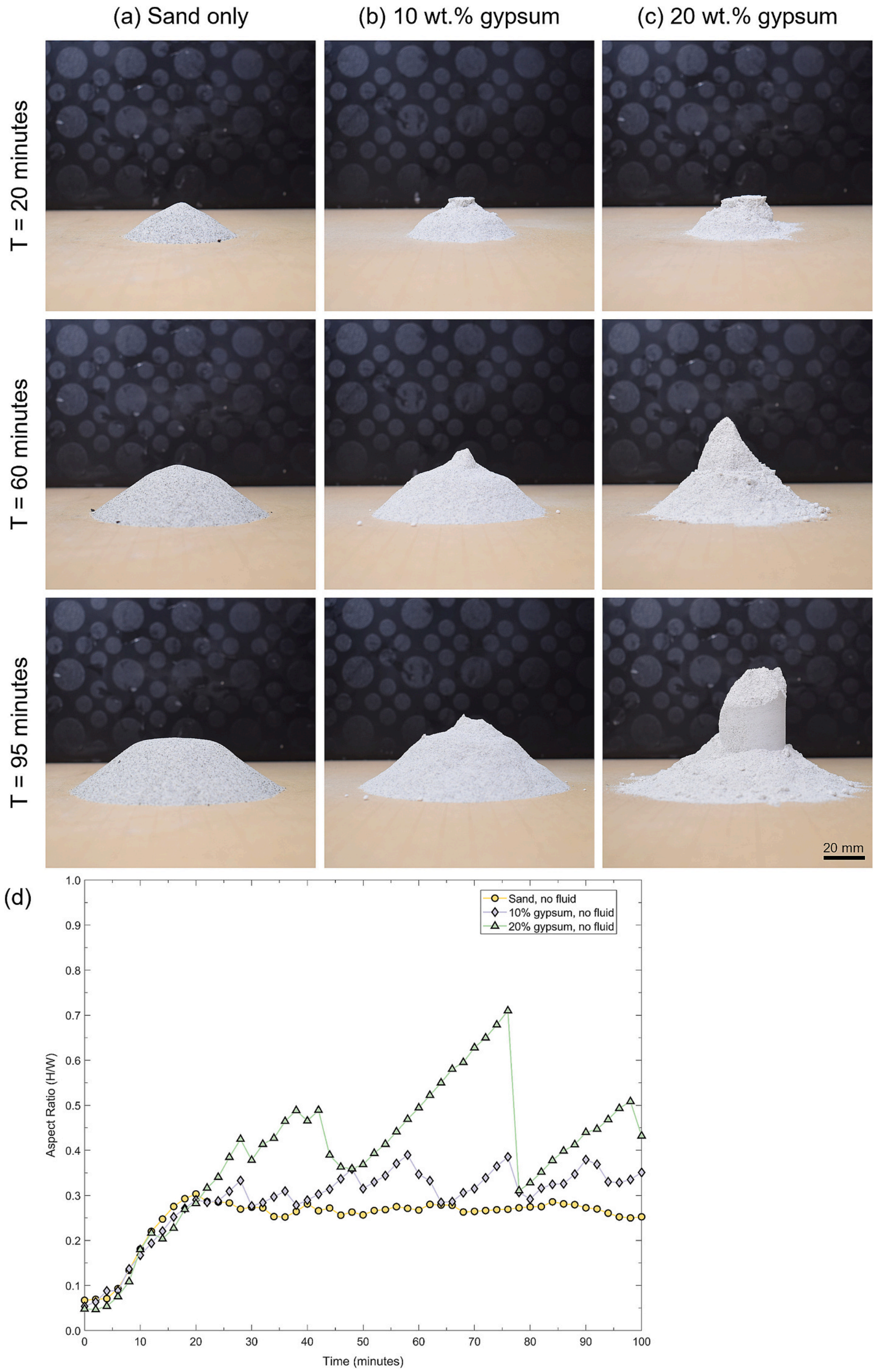

Fig. 6. Evolution of model domes and spines made with granular material only. Photographs from the models with **(a)** sand only; **(b)** sand with 10 wt% gypsum; **(c)** sand with 20 wt% gypsum taken at $T = 20$ min; $T = 60$ min; and $T = 95$ min since onset of piston motion. **(d)** Plot showing the aspect ratio through time of experiments with different gypsum plaster content. The characteristic sawtooth pattern corresponds to collapse events which see sudden reductions in height and increases in width.

was circular when viewed from above and had final dimensions of H = 33 mm, W = 119 mm, and AR = 0.28.

3.2.2. 10 wt% gypsum mixture with low viscosity fluid

Extrusion of a column of low-gypsum sand mixture and low viscosity fluid produced transient spiny protrusions from the dome top, followed by extrusion of a lobate fluid flow (Fig. 7b). As in the corresponding no-fluid experiment, extrusion of the granular material formed a series of short-lived spiny structures. The growth and collapse of these spines are reflected in the saw-tooth pattern of the dome aspect ratio evolution, which varied between 0.29 and 0.42 (Fig. 7d). These spines protruded to a maximum of ~10 mm above the upper dome surface before collapsing. At T = 70 min, the granular material had formed a dome-spine complex with dimensions H = 41 mm, W = 109 mm, and AR = 0.38 and the fluid began to intrude into the dome. The fluid broke through the surface of the dome-spine complex at $T = 75$ min, which was also when the dome-spine complex reached its maximum height of 44 mm. In the remaining 25 min of the experiment, the fluid continued to extrude and formed a

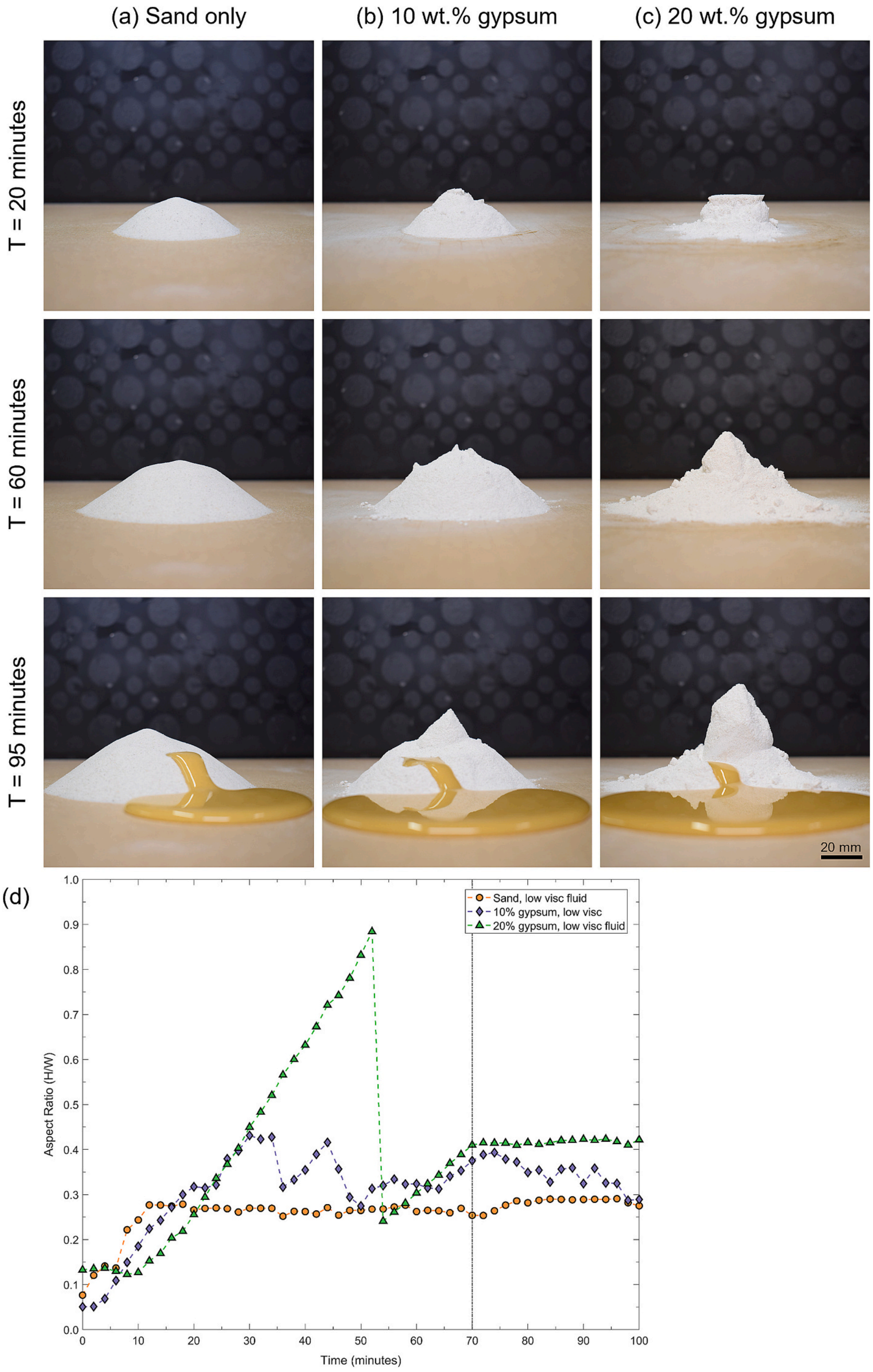

Fig. 7. (next page) Photographs from the models of (a) sand only; (b) sand + 10 wt% gypsum; (c) sand + 20 wt% gypsum taken at T = 20 min; T = 60 min; and T = 95 min. (d) Plot showing the aspect ratio through time of experiments with different gypsum plaster content. Vertical black line indicates time at which fluid reaches the top of the conduit.

lobate flow at the base of the dome (Fig. 7b). At *T* = 95 min, the spiny structure that had been present since T ~ 63 min started to break apart along a series of parallel sub-vertical fractures that accompanied rotation of the spine block to fill the space left by fluid extrusion. After 100 min, the dome-spine complex had final dimensions of H = 35 mm, W = 122 mm, and AR = 0.29.

3.2.3. *20 wt% gypsum mixture with low viscosity fluid*

Extrusion of a high-gypsum sand mixture and low viscosity fluid produced a large monolith structure before fluid broke through the granular mixture and formed a lobate flow around the base of the dome-spine complex (Fig. 7c). For the first 52 min of the experiment, a cohesive column of granular material extruded with a diameter equal to that of the internal conduit diameter (38.1 mm) to a height of 65 mm. Approximately 50 % of the material making up the monolith-like structure then collapsed, with the remaining column having a height of 33 mm. The steep and sudden decrease in aspect ratio from 0.88 to 0.24, as seen in Fig. 7d, is the result of this rapid collapse event. The fluid had reached the top of the conduit at *T* = 70 min and had broken through the granular material at *T* = 73 min. From *T* = 96 min until the end of the experiment, the spine block rotated to fill the space left behind by the extruding fluid, causing a large throughgoing fracture to form. After 100 min, the fluid had formed a lobate flow around the base of the dome-spine complex, which now had dimensions of H = 59 mm, W = 140 mm, and AR = 0.42.

3.3. *Granular material with a high viscosity fluid*

The next suite of experiments also used a two-material conduit. The bottom 45 mm of the conduit had a high viscosity fluid with 50 wt% sugar crystals. The remaining 105 mm of the conduit was filled with a granular mixture of sand and (a) 0 wt% gypsum; (b) 10 wt% gypsum; and (c) 20 wt% gypsum.

3.3.1. *Sand with high viscosity fluid*

Extrusion of a two-material column produced an axisymmetric dome of granular material from which a lobate fluid extrusion was observed (Fig. 8a). In the first 20 min of extrusion, the dome reached H = 19 mm and W = 74 mm. The dome continued to grow laterally by avalanching and maintained a near constant aspect ratio of 0.23–0.27. At *T* = 70 min

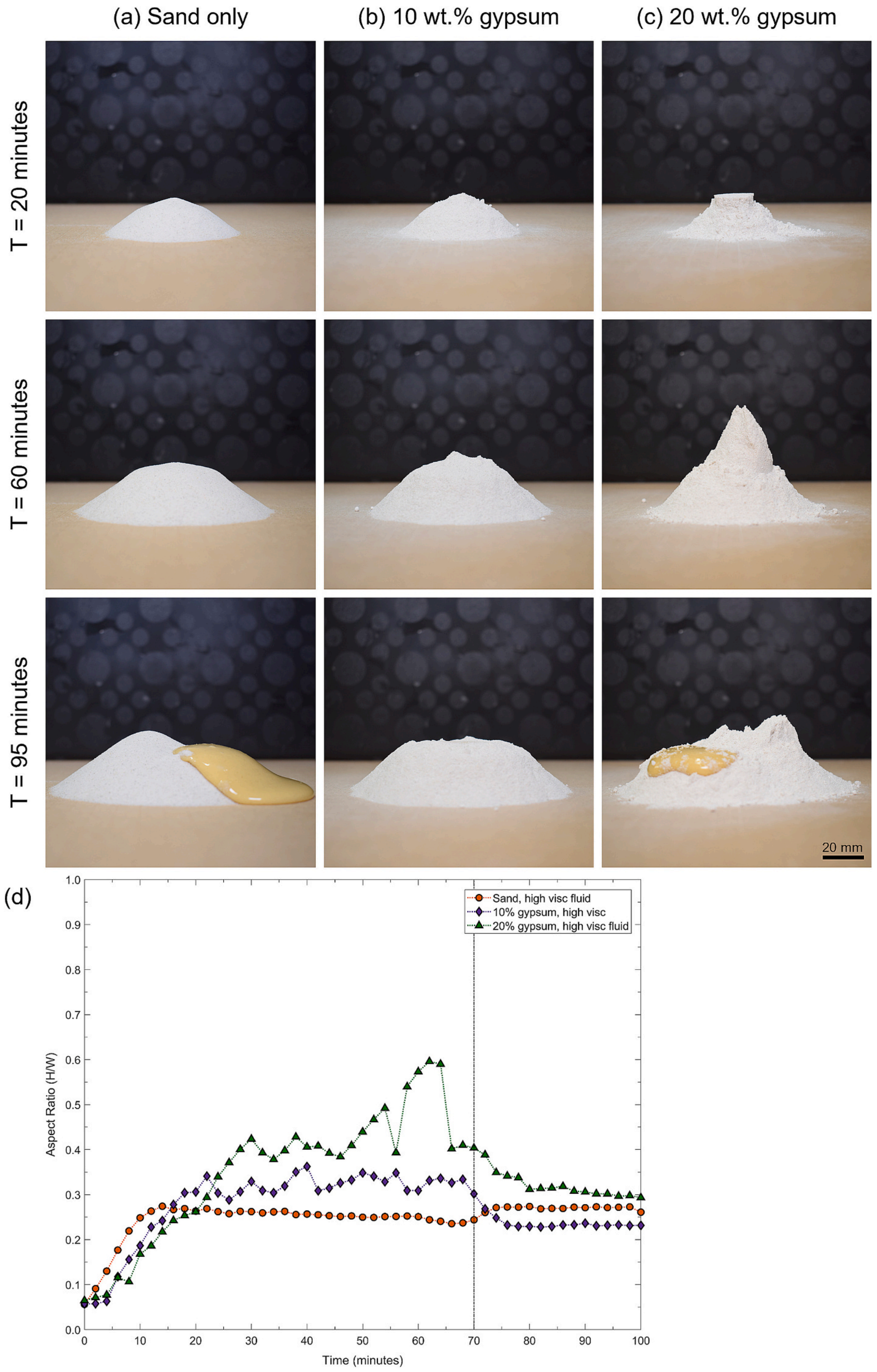

Fig. 8. (next page) Photographs from the models of (a) pure sand; (b) 10 wt% gypsum; (c) 20 wt% gypsum taken at T = 20 min; T = 60 min; and T = 95 min. (d) Plot showing the aspect ratio through time of experiments with different gypsum plaster content. Vertical black line indicates the time at which fluid should reach the top of the conduit.

(vertical dashed line in Fig. 8d), the granular portion of the column had been extruded and the fluid portion began intruding into the established dome, which at this time had grown to H = 28 mm and W = 116 mm with AR = 0.23. The dome height increased with the addition of fluid to the extrusion, leading to AR = 0.27. At *T* = 78 min, the fluid broke through the granular material (Fig. 8a). During the remainder of the experiment, fluid continued to extrude from the dome to form a lobate flow around the dome base. The final dome was circular when viewed from above and had dimensions of H = 32 mm, W = 121 mm, and AR = 0.26.

3.3.2. 10 wt% gypsum mixture with high viscosity fluid

Extrusion of a column of low-gypsum sand mixture and high viscosity fluid produced transient spiny protrusions from the dome top, followed by lateral spreading of the dome driven by the fluid intrusion into the granular pile (Fig. 8b). Consistent with observations from the no-fluid and the low viscosity fluid experiments, extrusion of sand with gypsum plaster formed a series of short-lived spiny structures which are reflected in the aspect ratio evolution (Fig. 8d). These spines protruded to a maximum of ~10 mm above the upper dome surface before collapsing. At T = 70 min, the granular material had formed a dome-spine complex with dimensions H = 33 mm, W = 110 mm, and AR = 0.30 and the fluid began to intrude into the dome. Growth continued endogenously, such that the fluid stayed contained within the dome (Fig. 8b). During this phase of the experiment, growth was dominated by lateral spread which we observed as an increased width and decreased height. The decrease in height is thought to occur due to the syrup pushing the upper surface outwards, causing gravitational over-steepening and collapse. After 100 min, the final dome-spine complex had dimensions of H = 29 mm, W = 126 mm, and AR = 0.23.

3.3.3. 20 wt% gypsum mixture with high viscosity fluid

Extrusion of a high-gypsum sand mixture and high viscosity fluid produced a large monolith structure before fluid broke through the granular mixture in the upper region of the flank and formed a short flow (Fig. 8c). For the first approximately 65 min of the experiment, a cohesive column of granular material extruded with a diameter equal to that of the internal conduit diameter (38.1 mm) to a height of 66 mm. During this time, there were a small number of very localised, small-volume failures that did not decrease the height of the main structure but added material to the base of the dome, thus increasing the width and decreasing the aspect ratio. These are observed as small drops in the calculated aspect ratio in Fig. 8d and differ from collapse-related aspect ratio changes since they occur less instantaneously (shallower gradient in Fig. 8d) and the absolute change in aspect ratio is smaller. By *T* = 66 min, a vertical fracture plane cut through the spine and resulted in one side of the spine slumping. At T = 70 min, the fluid had reached the top of the conduit and was pushing the overlying plug/spine material out to one side. At *T* = 88 min, motion of the spine block had ceased and the fluid had emerged at the surface of the dome along an approximately 60 mm arcuate fracture at the base of the spine block. From this point until the end of the experiment, fluid continued to extrude along the length of this fracture to form a short flow. After 100 min, the fluid had formed a flow covering ca. 20 % of the flank when viewed from above, with the dome-spine complex with dimensions of H = 42 mm, W = 142 mm, and AR = 0.29.

4. Discussion

4.1. Comparison with nature

We qualitatively compared images of lava domes and lava spines in nature to the images captured during each experiment (Fig. 9). We found that we were able to replicate the visual appearance of viscous extrusions in nature with both the models and natural examples having a similar AR. Model domes range from flat-topped extrusions, such as observed at Novarupta (Fig. 9a, e), to conical spiny domes such as seen at Kelud (Fig. 9b, f) and Paluweh (Fig. 9c, g), to columnar spines such as observed at Mt. Pelée (Fig. 9d, h).

We also compared the quantitative results of our experiments to data collated by Myers et al. (2024) that describe the geometry of viscous extrusions in nature (Fig. 10). Myers et al. (2024) collated 323 recorded measurements of viscous extrusions classified in past publications as lava domes or spines to generate a global dataset of extrusion height, width, and aspect ratio. They found that aspect ratios of viscous extrusions ranged from 0.02 to 3.17, with the structures described as spines typically exhibiting aspect ratios above 0.8. The modelled lava domes presented here have aspect ratios between 0.02 and 0.9 (Fig. 10) which captures ~90 % of the aspect ratio variation seen in nature.

The main mismatch between model and nature is that our models apparently underrepresent maximum spine height in nature. Model AR attained a maximum of 0.9, whereas values recorded in nature reach up to 3.0 (Fig. 10). We see monolith structures formed from highly cohesive granular material (Fig. 9d; AR ~ 0.5), that are qualitatively similar to the monolithic spine recorded at Mont Pelée (Martinique) in 1903 (Fig. 9h; AR ~ 2.4). The measurements shown in the solid symbols in

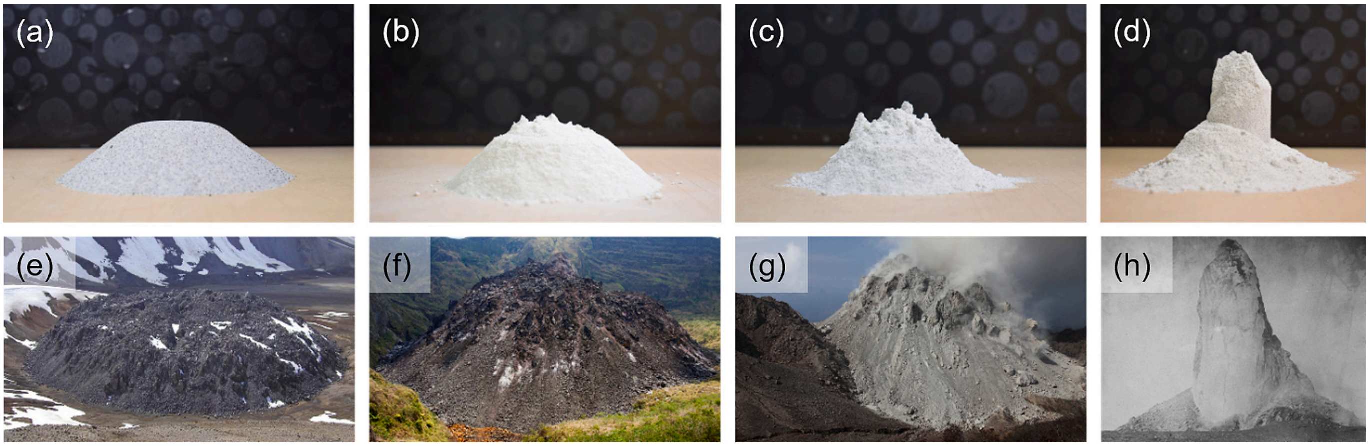

Fig. 9. Comparison of dome geometry and characteristics in experiments with examples in nature: **(a)** pure sand without viscous fluid (AR ~ 0.26); **(b)** 10 wt% sand-plaster mixture with viscous fluid (AR ~ 0.31); **(c)** 20 wt% sand-plaster mixture without viscous fluid (AR ~ 0.44); **(d)** experiment with 20 wt% sand-plaster mixture and no viscous fluid (AR ~ 0.5 if the width of the entire extrusion is measured; increases to AR ~ 1.5 if only the dimensions of the 'spine' are measured); **(e)** Novarupta lava dome, USA (AR ~ 0.18; photo by USGS); **(f)** Kelud lava dome, Indonesia (AR ~ 0.3; photo by Øystein Lund Andersen); **(g)** Paluweh lava dome, Indonesia (AR ~ 0.5; photo hosted by Photovolcanica); **(h)** Pelée spine, France in 1903 (AR ~ 2.4; photo from USGS).

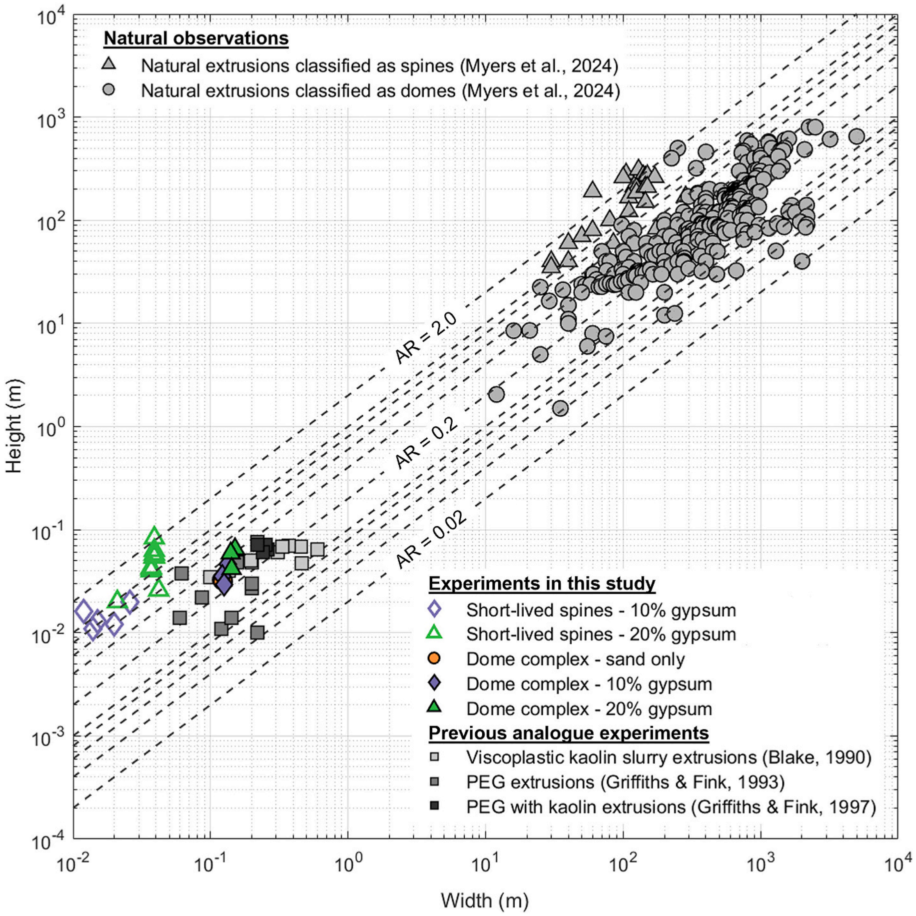

Fig. 10. Log-log plot of height and width measurements from viscous extrusions. Grey circles show natural domes and grey triangles show spines as classified in literature (from Myers et al., 2024). Coloured filled points show the final geometry in each experiment from this study, shown only as a function of cohesion for sand (orange circles), sand with 10 % gypsum (blue diamonds) and sand with 20 % gypsum (green triangles). Hollow symbols show maximum spine dimensions from short-lived spines for 10 % gypsum (diamonds) and 20 % gypsum (triangles). Grey squares show dimensions from previous viscoplastic analogue models (Blake, 1990; Griffiths and Fink, 1993; Griffiths and Fink, 1997). Dashed grey lines represent lines of equal aspect ratio. Note that despite the difference in absolute height and width values, modelled and natural extrusions have similar height-width aspect ratios and thus possess geometric similarity. (For interpretation of the references to colour in this figure legend, the reader is referred to the web version of this article.)

Fig. 10 underestimate spine aspect ratio. This is due to the measuring convention, where we measure the full dome complex rather than the spine itself. This is in contrast to measuring convention in the field, where lava spines are often measured as individual structures rather than as part of the larger complex they are associated with. To assess the effect of this measurement method, we manually calculated the dimensions of spines across our experiments (i.e., those with 10 % and 20 % gypsum). The new measurements are indicated by hollow symbols in Fig. 10 and reach aspect ratios up to 1.98. Conversely, including the talus from the base of the Mt. Pelée extrusion in the width measurement decreases the calculated aspect ratio from 2.4 to 0.8, which is consistent with the aspect ratios of high cohesion columnar extrusions produced in our experiments.

One finding by Myers et al. (2024) was evidence of a power law relationship governing the height and width of viscous extrusions in nature, shown by a straight-line relationship between height and width on a log-log plot. The results of our experiments lie on the same trend when we extend the plot to include centimetre-scale structures (Fig. 10). Given the strong quantitative and qualitative match between modelled and recorded viscous extrusions, we suggest that the models are well-scaled and show self-similar behaviour with natural systems.

4.2. Approaches to analogue modelling of lava domes and limitations of our study

Dome emplacement is controlled by several variables, including magma composition (e.g., chemistry, volatile content, crystallinity, and vesicularity), vent and conduit geometry, effusion rate, and effusion continuity (i.e., episodic vs. continuous growth). Modelling studies must choose an appropriate simplification of these variables, such that model results are both practical to attain and informative on the dynamics of the extrusion process. Past lava dome modelling studies can be broadly grouped into (i) those that considered an isothermal system, whereby the effects of fluid or solid mechanical properties were explored at constant temperature (e.g. Huppert et al., 1982; Blake, 1990; Buisson and Merle, 2005; Zorn et al., 2020; this study), and (ii) those that consider a temperature-dependent system, whereby thermo-mechanical effects during dome growth were investigated also (Griffiths and Fink, 1993; Fink and Bridges, 1995; Griffiths and Fink, 1997; Fink and Griffiths, 1998).

Past isothermal analogue models of lava domes have used various analogue materials, the rheologies of which encompass viscous Newtonian fluids (Huppert et al., 1982; Buisson and Merle, 2002; 2005), visco-plastic Bingham fluids (Blake, 1990), and frictional-plastic granular solids (Buisson and Merle, 2005; Zorn et al., 2020). All have considered extrusion of the model material onto a horizontal surface.

Newtonian fluids were silicon oils or polymers. Bingham fluids have comprised water-kaolin slurries of varying density, viscosity and yield strength (parameters that are positively correlated). Granular materials have comprised quartz sand with or without some finer grained filler, such as flour or gypsum powder, as used in our study.

Depending on emplacement rate and viscosity, isothermal fluid-based analogue models have typically produced domes with aspect ratios ranging from ~0.1 to 0.35 (Huppert et al., 1982; Blake, 1990; Buisson and Merle, 2002). In general, dome aspect ratios decreased continuously during an experiment as the dome grew. Experiments with Newtonian fluids show continuous spreading with a corresponding decrease in AR to extremely low values <0.01 (Huppert et al., 1982), whereas experiments with visco-plastic (Bingham) fluids have a yield strength that inhibits and ultimately ceases flow. These fluid-only domes are characterised by relatively smooth, semi-circular to parabolic cross-sectional profiles. The relatively low aspect ratio and smoothness of the fluid-only isothermal domes led researchers (e.g., Blake, 1990; Griffiths and Fink, 1997) to conclude that higher aspect ratios and spinier morphologies in nature (Figs. 1 and 9) might be accounted for by: (i) a stronger material (brittle or viscous 'crust') at the dome margins; (ii) a more solid, brittle rheology within the dome overall; and/or (iii) the presence of a friction-controlled talus/rubble apron surrounding the dome margins.

Within an isothermal framework, models incorporating brittle to frictional plastic granular materials (Buisson and Merle, 2005; Zorn et al., 2020; this study) have attempted to capture the characteristics of higher aspect ratio domes and spines. Buisson and Merle (2005) extruded a silicone polymer dome, which they then covered with a sand-flour carapace to simulate cooling and crust formation during extrusion. Zorn et al. (2020) went further by treating the entire dome as an extruding granular solid and by varying the material strength via the sand-gypsum ratio, as in our study. This approach generated, for all material strengths, a volumetrically substantial talus apron. Blake (1990) suggested that the angle of repose of the talus controls the slope of the dome margins. This is corroborated in our models where slope angle increases with increased plaster content and relates to increased residual frictional strength of the failed material (cf. Figs. 6 & 7 of Poppe et al., 2021). Our low-strength modelled domes have marginal slopes of ~30° and have a classic flat-topped cross-section profile observed at many domes in nature. This flat top is generated as upthrust low-strength material rapidly disintegrates and spalls over the dome flanks to become part of the talus apron. Higher strength material remains intact for greater uplift magnitudes, and strain localises onto conical or cylindrical shear zones within the dome (Zorn et al., 2020), such that intact spines emerge from the dome top. At the highest strengths, these spines are columnar and dominate the extrusion before eventually becoming unstable and collapsing (see also Section 4.3). The high-strength domes in our models frequently had marginal slopes of up to 45°, as is common at many Peléean-style domes in nature (Blake, 1990). In addition to replicating the spiny to monolithic cross-section profiles in nature, high to extremely high aspect ratios of 0.9–2.8 (depending on measuring convention) are also attained. As such, consideration of lava dome growth in terms of isothermal extrusion of a frictional plastic granular solid has produced results able to explain a range of dome and spine phenomena that eluded past isothermal fluid-only models.

Thermo-mechanical analogue models of lava domes offer an alternative approach for attaining a range of dome aspect ratios and morphologies. Previous laboratory studies have centred on the extrusion and solidification of initially molten PEG wax, either alone (Griffiths and Fink, 1993; Fink and Bridges, 1995), or with added kaolin powder in suspension (Fink and Griffiths, 1998; Griffiths and Fink, 1997). Use of PEG wax allows for a Bingham fluid behaviour with formation of a solid crust upon cooling. The wax viscosity varied by less than a factor of two over the temperature range investigated. A key finding from these experiments was that the ratio of cooling rate to eruption rate controlled the morphology and dynamics of dome extrusion. This finding was also linked to continuity of fluid extrusion (Griffiths and Fink, 1993). For example, if a dome grows over several episodes between which cooling can occur, then the long-term evolution of the dome is characterised by a high time-averaged cooling rate relative to the time-averaged eruption rate and thus exhibits a higher aspect ratio. The schematic in Fig. 11 shows dome morphologies considering the ratio of eruption to cooling rate for either continuous or discontinuous eruptions. With wax-only experiments (Fink and Bridges, 1995), typical aspects ratios produced during continuous extrusion were 0.02–0.33. Dome aspect ratios produced with episodic extrusion were slightly higher on average at 0.1–0.38, although two experiments involving slow episodic extrusion at near solidus temperature produced aspect ratios of 0.6–0.8 (Fink and Griffiths, 1990). The morphological features produced in modelled wax domes included bulbous pillow-like protrusions at high cooling rates, rifted plates and folds at intermediate cooling rates, and flow levees at low cooling rates (Griffiths and Fink, 1993). Where cooling rate was low relative to eruption rate, dome morphologies were axisymmetric and similar to those produced by Blake (1990) using isothermal kaolin slurries. Where the cooling rate was high relative to the eruption rate in models with wax-clay mixtures, the dome was more likely to have a lobate or spiny surface morphology, although aspect ratios mainly remained in the range of 0.2–0.35 (Fink and Griffiths, 1998).

The isothermal approach as explored in our study is complementary to previous thermo-mechanical studies if one considers thermal effects to occur mostly in the shallow conduit during repose periods, rather than operating mostly after extrusion at the surface. The red lines in Fig. 11 show episodic dome growth, whereby cooling can occur either at the surface as explored by Fink and Bridges (1995) or during residence of magma within the conduit as assumed here. Both cases are equivalent to a long-term time-averaged extrusion rate that is low relative to a high cooling rate, as in previous thermomechanical studies (Fink and Bridges, 1995; Fink and Griffiths, 1998). Although our models do not explicitly include temperature or temperature-dependent material behaviour, they implicitly consider a long-term change in material properties due to either pre-eruptive thermal effects in the conduit after a pause in extrusion, or to processes (e.g., degassing) that push the extruding material from visco-plastic to frictional plastic behaviour. This means that material erupted during early extrusion behaves as a brittle solid and is then followed by eruption of viscous magma from depth.

In our models, the sand-gypsum mix therefore represents cooled upper conduit material which is extruded either at the beginning of a dome-forming eruption after quiescence or the beginning of a new active phase during episodic extrusion. We consider that varying the gypsum proportion therefore represents the mechanical consequence of magma residence time, such that higher gypsum content produces a stronger material, representative of a denser, more crystalline, likely cooler magma after a longer repose period.

Dome growth is often classified as either exogenous or endogenous. Exogenous growth refers to lava emplacement at the surface adjacent to the vent (i.e., through lobe formation), whereas endogenous growth occurs when fresh dome material intrudes into the interior of an existing dome, causing inflation and surface deformation. We suggest that our models initially show exogenous growth, where spines grow and collapse, and new spines grow on top of the collapse deposits. When fluid reaches the top of the conduit, we see endogenous growth (e.g., see Section 3.3.2) where the dome surface inflates until the fluid breaks through the solid talus to reach the surface (see also Section 3.3.3) and exogenous growth resumes. Observations of the 1980–1986 Mount St. Helens eruption also showed that early episodes were dominated by exogeneous lobe formation, followed by the retention of increasing amounts of magma within the dome during later episodes; this is logical because a smaller dome has limited internal space in which to accommodate new magma before fracturing (Fink and Anderson, 2023).

The transition from exogenous to endogenous growth at Mount St. Helens has been attributed to (1) a shift in magma composition due to injection of new magma at depth (Swanson and Holcomb, 1990); (2) a

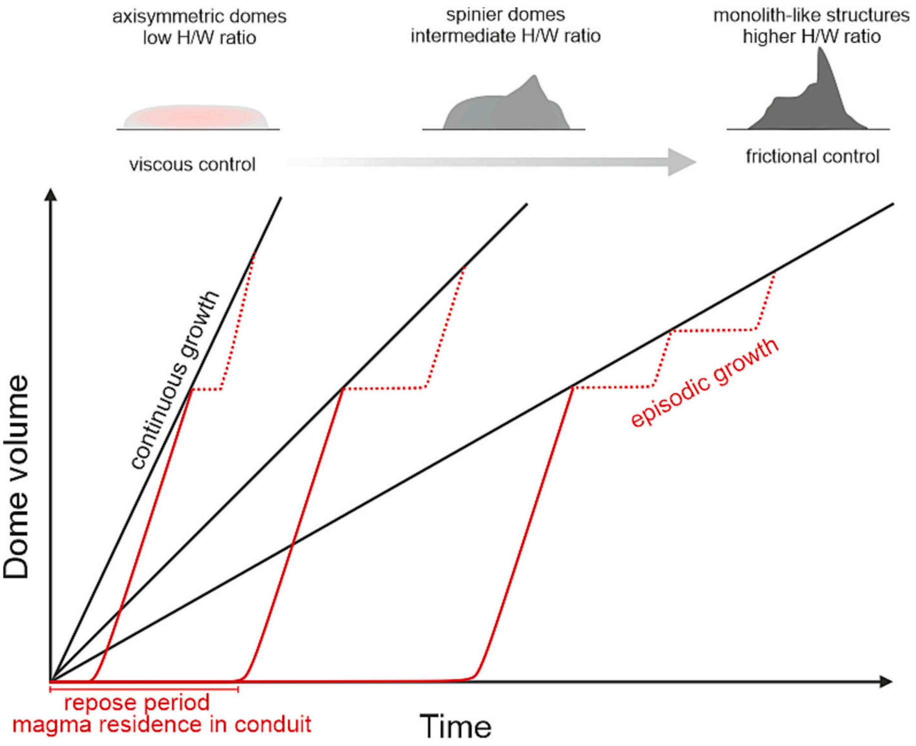

Fig. 11. A schematic figure to show possible dome growth trajectories considering continuous (black) and episodic (red) dome growth. High eruption rates relative to low cooling rates typically produce low aspect ratio, axisymmetric domes. Higher cooling rates produce spinier domes. Longer repose periods lead to higher cohesion material in the conduit.

decrease in magma intrusion rate due to magma crystallisation within the conduit; and (3) an inward migration of isotherms within the dome, such that the outer dome crust must be broken for exogenous lobes to form. Whilst the varied viscosity across our different models may relate to different magma compositions, we do not vary fluid viscosity within one experiment. We also do not simulate different eruption rates or the explicit evolution of mechanical properties due to time-dependent solidification and increasing yield strength of the fluid portion of our experiment. We show an increase in yield strength through increasing cohesion of the sand-plaster mix. Spiny surface morphology resulting from increased cohesion has also been achieved in previous experiments through use of a material with a temperature-dependent rheology and reduction of the ratio of extrusion rate to cooling rate (Fink and Bridges, 1995; Fink and Griffiths, 1998). We suggest integration of the earlier approaches and our approach (i.e., temperature dependent rheology, variation of extrusion rate, but inclusion of a higher cohesion granular material) may allow an integrated exploration of a wider spectrum of dome morphologies.

The experimental setup presented here uses a steel pipe conduit, analogous to cylindrical conduits typical of summit domes, such as those at Volcán de Colima (e.g., Walter et al., 2019) or Mount St. Helens (e.g., Vallance et al., 2008). We acknowledge that conduit geometry in nature could be much more complex and influence extrusion (e.g., Mériaux et al., 2022; Walter et al., 2022). For example, volcanic dome sequences have also been found to occur in linear or arcuate arrays, indicating that they are fed by dikes, such as those at Medicine Lake Highland Volcano, USA (Fink and Pollard, 1983; Luhr and Carmichael, 1980). These domes fed by tabular conduits are often elongate parallel to the dike alignment, such that their morphologies likely differ from the axisymmetric domes presented here. Dike-fed domes also do not typically experience the episodic growth that we simulate here.

Finally, we suggest that future studies should incorporate photogrammetric analysis at each timestep. From this, digital elevation models can be generated to enable estimation of the evolution of extrusion volume and morphology in greater detail.

4.3. *The roles of cohesion and viscosity in dome growth and deformation*

Increasing the gypsum plaster content in the granular solid from 0 wt % to 20 wt% creates a more cohesive material capable of supporting taller structures with steeper sides. As such, we observed more localised, brittle fracturing through the experiment, with the scale of fractures increasing with the cohesion of the granular plug. The addition of gypsum plaster shifted the growth style from material spalling and small avalanches on the slopes of an axisymmetric dome toward extrusion of tall monoliths. These monoliths typically had widths defined by the conduit diameter. In the experiments with high cohesion, increase in dome width commonly occurred via spine collapse. These collapses occurred through two main mechanisms (Fig. 12): (1) generation of throughgoing fractures that led to detachment and outward toppling of the spine block (Fig. 12 **a-c**); and (2) progressive oversteepening of the spine that eventually slumped along an approximately planar failure surface (Fig. 12 **d-f**). Both mechanisms of spine failure have been documented in natural systems. For example, cracks developed along the axis of several spines of the 2004–2006 Mount St. Helens dome complex, followed by decoupling of the spine from the source and eventual toppling and disintegration (Vallance et al., 2008). Gravitational oversteepening and slumping of spines was also observed during the early stages of the Soufrière Hills eruption (Watts et al., 2002).

Extrusions of higher-cohesion material produce spines whereas lower cohesion material produces blockier, lower aspect ratio domes. This has been shown in comparison between the Mount St. Helens dome that formed in the crater during the 1980–1986 eruption and the domes formed during the 2004–2008 eruption. This hypothesis has been tested by comparing the dacite lavas that formed a flat-topped dome during 1980–1986 with those that formed the spines and whalebacks erupted in 2004–2008. Heap et al. (2016) showed that the 1980–1986 dacite had higher porosity, and was therefore weaker, than the low porosity dacite

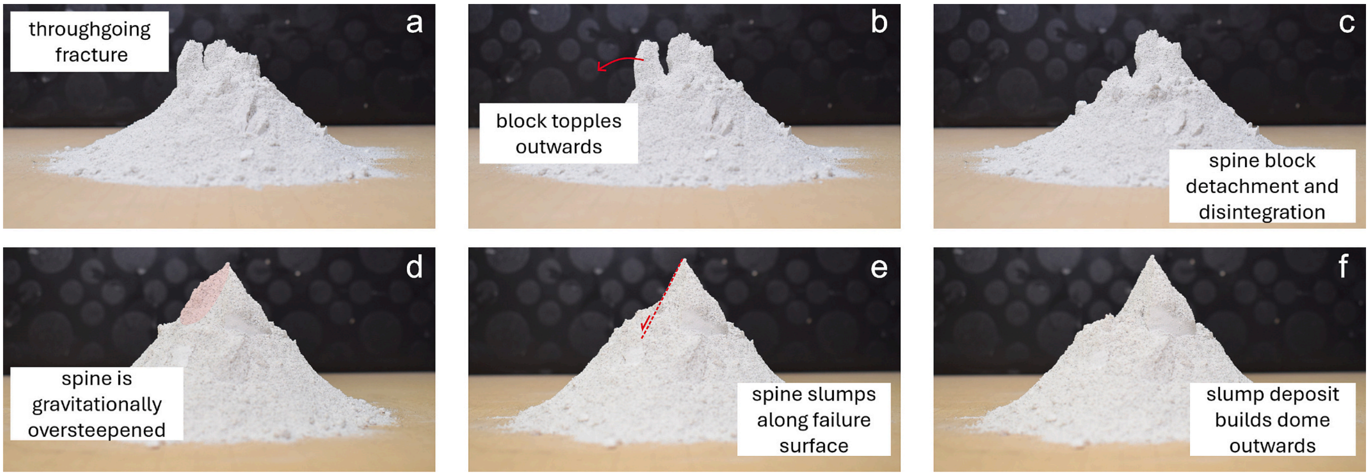

Fig. 12. Modes of spine collapse. (a-c) show formation of a throughgoing fracture that enables toppling of a spine block away from the remaining spine, taken from the 20 % gypsum, no fluid experiment. (d-f) show gravitational oversteepening of the spine, followed by slumping, taken from the 20 % gypsum, high viscosity fluid experiment.

erupted in 2004–2008. The porous 1980–1986 dacite also transitioned to ductile behaviour at low pressure, whereas the low-porosity 2004–2008 dacite was brittle even at high pressure. Using these data, these authors hypothesised that porosity and crystal content (i.e., glass content) controlled dome morphology: high porosity and low crystal content lava would create domes, and low porosity and high crystal content lava could create spines. Our mixtures with increased gypsum contents are analogous to the strong, crystalline, spine-forming materials observed in nature.

With the addition of a low-viscosity fluid, the model extrusions overall exhibited the same growth behaviours as those noted for extrusions without any fluid. A subtle effect of the fluid was seen when it reached 20 mm from the top of the conduit and started to influence deformation behaviour of the material already extruded by suppressing spine formation. The lack of spines once fluid enters the dome was most visible in the high-cohesion example (Fig. 7d), which, when compared to

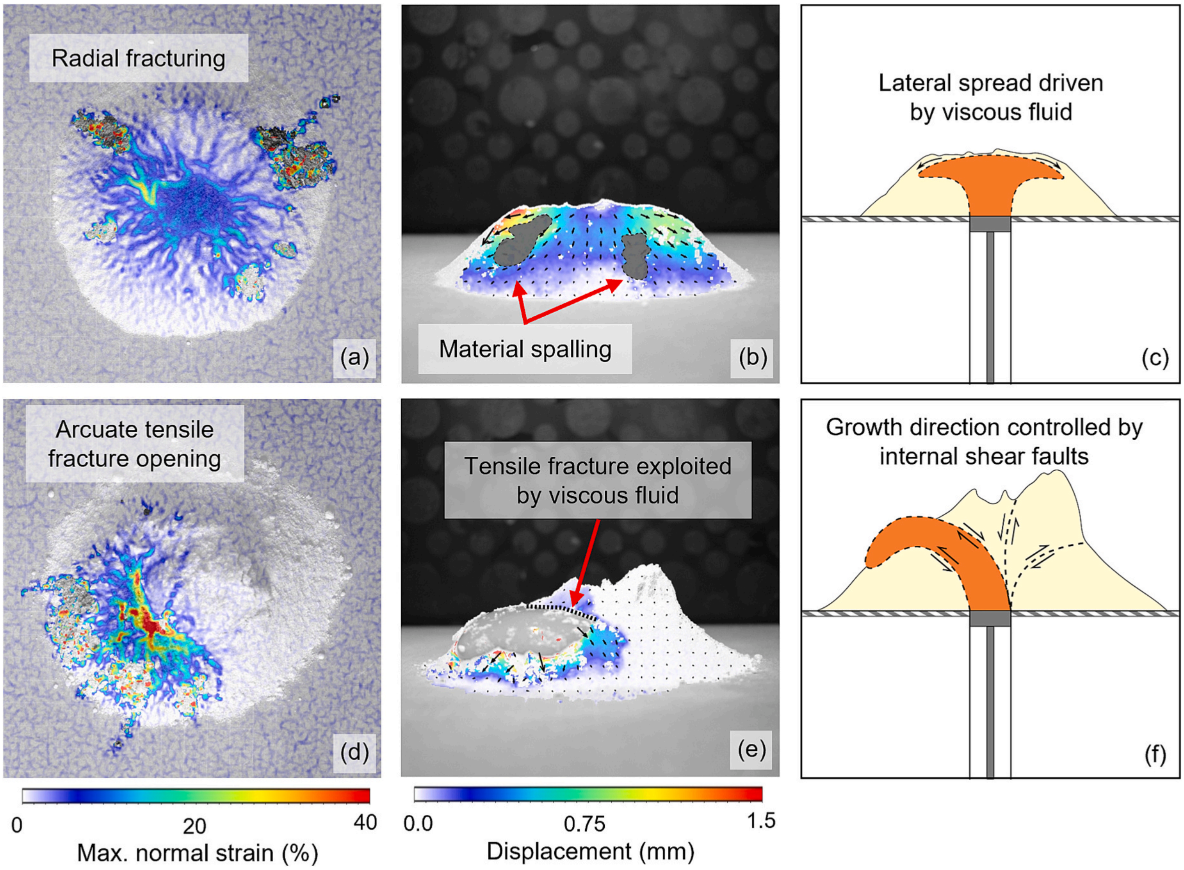

Fig. 13. Results of Particle Image Velocimetry (PIV) showing model deformation and conceptual cross-sections. Comparison of the high-viscosity fluid and sand plaster mixture with **(a, b, c)** 10 wt% gypsum and **(d, e, f)** 20 wt% gypsum. **(a, d)** show maximum normal strain at T = 90 min, when no fluid is present at the surface of the dome. **(b, e)** show displacement at T = 95 min. **(c, f)** show conceptual sketches illustrating internal structures controlling extrusion morphology.

the same experiment with no fluid present (Fig. 6d), showed the absence of saw-tooth AR changes due to spine extrusion and collapse, as well as a significantly reduced AR in the late stage of the experiment. We suggest this is because the spreading of the viscous fluid is dominantly outward, so there is insufficient vertical force to produce spines. The experiment with low-viscosity fluid also led to the formation of flows resembling exogenous lava lobes or coulées at all gypsum plaster concentrations. We suggest this is due to the interplay between viscosity and cohesion; highly cohesive materials become more extensively fractured which provides a pathway that the fluid can exploit. This may be similar to the formation of lobes at Unzen during the 1990–1995 eruption, where cracks were observed at the summit of the dome followed by extrusion of several successive lobes (Kaneko et al., 2002).

Increasing the viscosity of the fluid used in the experiments led to a more fluid being retained within the dome. We observe lateral spreading of the dome prior to fluid breakout, generating final dome morphologies with lower AR than their low-viscosity and no-fluid equivalents. Fig. 13 shows results of PIV of strain at $T = 90$ min (Fig. 13a, d) and displacement at $T = 95$ min (Fig. 13b, e). The strain shows radial fracturing in the case of 10 wt% gypsum (Fig. 13a) compared with the localisation of arcuate tensile fractures for 20 wt% gypsum (Fig. 13d). In the model using a 10 wt% sand-plaster mixture (Fig. 13a,c), the dome maintained an axisymmetric form once fluid reached the upper conduit and suppressed spine formation. Outwards spreading of material in the uppermost portion of the dome can be seen in displacement vectors that are oblique to the slope. Material spalling on the flanks produced regions of image decorrelation in Fig. 13b. In contrast, the fluid is not contained within the dome for the entirety of the experiment using a 20 wt% sand-plaster mixture (Fig. 13e). Instead, deformation becomes focused in one region of the dome, with the fluid exploiting the arcuate fractures resulting in late-stage extrusion (Fig. 13d). Based on the observations made from both the time-lapse photographs and PIV analysis, we interpret the internal structure of these modelled domes to resemble the conceptual sketches in Fig. 13c and f.

The regimes of surface fracturing (i.e., fractures that are not contained within a spine; Fig. 12) can therefore be summarised as (1) radial tensile fracturing in intermediate cohesion material due to addition of material to the dome; and (2) arcuate tensile fracturing at the dome in high cohesion material. Conjugate radial surface fractures were also observed during endogenous dome growth in the laboratory studies by Griffiths and Fink (1997). Particularly in our high cohesion experiments, fracturing allows fluid to reach the surface and facilitates transition from endogenous to exogenous growth. We typically only observe fracturing at the top dome surface (Fig. 13) and not toward the talus slopes. This finding agrees with Denlinger (1990), who showed that fracturing is more likely to occur at the top of the dome than on the flanks due to the distribution of tensile stresses. This was also observed during the 1980–1986 eruption of Mount St. Helens (Fink and Anderson, 2023) and supported late-stage exogenous lobes originating from the dome's apex (see also Section 4.2). Spines have been shown in previous granular analogue experiments to grow through localization of deep-seated shear fractures within the dome (Zorn et al., 2020; Walter et al., 2022). Our study shows that these same shear fractures likely relate to the arcuate fractures we observe at the surface and that allow fluid to reach the surface (Fig. 13f).

4.4. *Implications*

The results of our analogue models highlight the importance of understanding fracture localisation at the surface and within a lava dome. We observed the formation of both radial and concentric fracture networks in the dome surface, the number and size of which in nature have implications on both the pathway viscous material is guided along during extrusion (e.g., Hale and Wadge, 2008; Zorn et al., 2019) and how efficiently the conduit magma can outgas (e.g., Hutchison et al., 2013; Moussallam et al., 2017). In instances where a lava dome is fractured, it is likely that a larger volume of volatiles can be lost from the magma, thereby inducing crystallisation, which acts to increase the viscosity of the magma and impart longer residence times onto packets of migrating magma (e.g., Zeinalova et al., 2021). Efficient outgassing is also thought to temper explosive behaviour (e.g., Cassidy et al., 2018). For example, whilst conduit-margin faults were considered as outgassing pathways during the 2004–2008 extrusion of lava spines at Mount St. Helens in the USA (Gaunt et al., 2014), the flat-topped lava dome and coulée that formed at La Soufrière in St Vincent (Eastern Caribbean) was ultimately destroyed by sub-Plinian explosions (Stinton, 2024).

Additionally, knowledge of factors such as residence time could help inform the structures most likely to form if a new extrusive episode were to occur. Since a longer residence time can promote formation of a plug with high crystal content and therefore high cohesion (e.g., Heap et al., 2016; Nakada and Motomura, 1999; Ryan et al., 2018; Smith et al., 2011), early-stage dome growth evolution may more closely resemble monolith end-member geometries, which are prone to potentially devastating collapse, as opposed to lateral spreading.

Further studies should investigate the potential of analogue modelling approaches to inform probabilistic hazard forecasting at dome-forming volcanoes. Our results suggest a link between the cohesive strength of plug-forming material and the frequency and magnitude of collapse events, whereby more cohesive mixtures underwent fewer but larger collapses compared to less cohesive mixtures. Analogue models may therefore prove to be particularly useful in understanding growth and collapse cycles of lava spines since these structures in nature are short-lived due to their inherent instability.

5. Conclusions

The salient conclusions of our study are as follows:

(1) Cohesion of solid dome or spine forming material occupying the upper part of the pre-eruptive conduit exerts the largest control on the first-order geometric parameters (height, width, and height-width aspect ratio) of viscous lava during onset of new dome growth.
(2) Viscosity of the fluid material in the pre-eruptive conduit plays a minor role in controlling the geometric form of viscous extrusions, particularly during onset of new dome growth.
(3) Dome growth is influenced by the interplay between cohesion and viscosity, whereby high viscosity fluid and an intermediate cohesion can lead to fluid retention within the dome and increased lateral spreading. Low viscosity fluid is able to flow through fractures within the talus and erupt at the surface.

Overall, our models suggest quantitative and qualitative geometric similarity to viscous extrusions in nature. By systematically varying rheological parameters within the dome, we can assess the delicate interplay between cohesion and viscosity on the growth and deformation behaviour of the dome during early growth. Therefore, our models can provide insight into the processes active in early extrusion when growth in nature is often missed due to the transient nature of lava spines and the small size of the early extrusion.

CRediT authorship contribution statement

Amy J. Myers: Writing – original draft, Visualization, Software, Methodology, Investigation, Formal analysis, Conceptualization. **Claire E. Harnett:** Writing – review & editing, Supervision, Project administration, Methodology, Funding acquisition, Conceptualization. **Eoghan P. Holohan:** Writing – review & editing, Supervision, Methodology, Conceptualization. **John G. Ryan:** Visualization, Methodology. **Edgar U. Zorn:** Writing – review & editing, Visualization, Formal analysis. **Thomas R. Walter:** Writing – review & editing. **Michael J. Heap:** Writing – review & editing.

Declaration of competing interest

C.E.Harnett reports financial support was provided by Royal Irish Academy. If there are other authors, they declare that they have no known competing financial interests or personal relationships that could have appeared to influence the work reported in this paper.

Data availability

Zenodo link included in manuscript

Acknowledgements

AM and CEH acknowledge funding from a UCD Ad Astra Fellowship and HEA Covid Fund, as well as support from a Charlemont Grant from the Royal Irish Academy. MJH acknowledges support from the Institut Universitaire de France (IUF). We acknowledge help from Alexis Hrysiewicz (UCD) for help with Matlab, Kevin Nolan for help with the viscometry, and Paul Cuffe for help with Arduino. We would like to thank Jonathan Fink and Karoly Nemeth for their insightful and helpful reviews that improved this manuscript.

Appendix A. Supplementary data

Supplementary data to this article can be found online at https://doi.org/10.1016/j.jvolgeores.2024.108196.

References

Barenblatt, G.I., 2003. Scaling, Cambridge University Press, Cambridge. https://doi.org/10.1017/cbo9780511814921.

Blake, S., 1990. Viscoplastic models of lava domes, lava flows and domes. In: IAVCEI Proceedings in Volcanology, pp. 88–126. https://doi.org/10.1007/978-3-642-74379-5_5.

Buisson, C., Merle, O., 2002. Experiments on internal strain in lava dome cross sections. Bulletin of volcanology 64, 363–371.

Buisson, C., Merle, O., 2005. Influence of crust thickness on dome destabilization. In: Manga, M., Ventura, G. (Eds.), Kinematics and Dynamics of Lava Flows: Geological Society of America Special Paper, 396, pp. 181–188. https://doi.org/10.1130/2005.2396(12).

Calder, E.S., Luckett, R., Sparks, R.S.J., Voight, B., Druitt, T.H., Kokelaar, B.P., 2002. Mechanisms of Lava Dome Instability and Generation of Rockfalls and Pyroclastic Flows at Soufrière Hills Volcano, Montserrat, the Eruption of Soufrière Hills Volcano, Montserrat from 1995 to 1999. Geological Society of London, pp. 173–190. https://doi.org/10.1144/gsl.Mem.2002.021.01.08.

Calder, E.S., Lavallée, Y., Kendrick, J.E., Bernstein, M., 2015. Lava dome eruptions. In: The Encyclopedia of Volcanoes. Academic Press, pp. 343–362.

Cassidy, M., Cole, P.D., Hicks, K.E., Varley, N.R., Peters, N., Lerner, A.H., 2015. Rapid and slow: varying magma ascent rates as a mechanism for Vulcanian explosions. Earth Planet. Sci. Lett. 420, 73–84. https://doi.org/10.1016/j.epsl.2015.03.025.

Cassidy, M., Manga, M., Cashman, K., Bachmann, O., 2018. Controls on explosive-effusive volcanic eruption styles. Nat. Commun. 9 (1), 2839. https://doi.org/10.1038/s41467-018-05293-3.

Castruccio, A., Rust, A.C., Sparks, R.S.J., 2010. Rheology and flow of crystal-bearing lavas: Insights from analogue gravity currents. Earth Planet. Sci. Lett. 297 (3–4), 471–480. https://doi.org/10.1016/j.epsl.2010.06.051.

Cole, P.D., Calder, E.S., Druitt, T.H., Hoblitt, R., Robertson, R., Sparks, R.S.J., Young, S. R., 1998. Pyroclastic flows generated by gravitational instability of the 1996–97 Lava Dome of Soufriere Hills Volcano, Montserrat. Geophys. Res. Lett. 25 (18), 3425–3428. https://doi.org/10.1029/98gl01510.

Denlinger, R.P., 1990. A model for dome eruptions at Mount St. Helens, Washington based on subcritical crack growth. In: *Lava flows and domes: emplacement mechanisms and hazard implications*. Springer Berlin Heidelberg, Berlin, Heidelberg, pp. 70–87.

Fink, J.H., Anderson, S.W., 2000. Lava domes and coulees. Encyclop. Volcan. 307–319.

Fink, J., Anderson, S., 2023. Lessons learned from the 1980–1986 eruption of the Mount St. Helens composite lava dome. Bull. Volcanol. 85 (6), 35.

Fink, J.H., Bridges, N.T., 1995. Effects of eruption history and cooling rate on lava dome growth. Bull. Volcanol. 57 (4), 229–239. https://doi.org/10.1007/s004450050091.

Fink, J.H., Griffiths, R.W., 1990. Radial spreading of viscous-gravity currents with solidifying crust. J. Fluid Mech. 221, 485–509.

Fink, J.H., Griffiths, R.W., 1998. Morphology, eruption rates, and rheology of lava domes: Insights from laboratory models. J. Geophys. Res. Solid Earth 103 (B1), 527–545. https://doi.org/10.1029/97jb02838.

Fink, J.H., Pollard, D.D., 1983. Structural evidence for dikes beneath silicic domes, Medicine Lake Highland Volcano. Calif. Geol. 11 (8), 458–461.

Galland, O., Holohan, E., van Wyk de Vries, B., Burchardt, S., 2018. Laboratory modelling of volcano plumbing systems: a review, physical geology of shallow magmatic systems. Adv. Volcanol. 147–214. https://doi.org/10.1007/11157_2015_9.

Gaunt, H.E., Sammonds, P.R., Meredith, P.G., Smith, R., Pallister, J.S., 2014. Pathways for degassing during the lava dome eruption of Mount St. Helens 2004–2008. Geology 42 (11), 947–950. https://doi.org/10.1130/g35940.1.

Griffiths, R.W., Fink, J.H., 1993. Effects of surface cooling on the spreading of lava flows and domes. J. Fluid Mech. 252, 667–702. https://doi.org/10.1017/S0022112093003933.

Griffiths, R.W., Fink, J.H., 1997. Solidifying Bingham extrusions: a model for the growth of silicic lava domes. J. Fluid Mech. 347, 13–36. https://doi.org/10.1017/S0022112097006344.

Hale, A.J., 2008. Lava dome growth and evolution with an independently deformable talus. Geophys. J. Int. 174 (1), 391–417. https://doi.org/10.1111/j.1365-246X.2008.03806.x.

Hale, A.J., Wadge, G., 2008. The transition from endogenous to exogenous growth of lava domes with the development of shear bands. J. Volcanol. Geotherm. Res. 171 (3), 237–257. https://doi.org/10.1016/j.jvolgeores.2007.12.016.

Harnett, C.E., Heap, M.J., 2021. Mechanical and topographic factors influencing lava dome growth and collapse. J. Volcanol. Geotherm. Res. 420, 107398. https://doi.org/10.1016/j.jvolgeores.2021.107398.

Harnett, C.E., Thomas, M.E., Purvance, M.D., Neuberg, J., 2018. Using a discrete element approach to model lava dome emplacement and collapse. J. Volcanol. Geotherm. Res. 359, 68–77. https://doi.org/10.1016/j.jvolgeores.2018.06.017.

Harnett, C.E., Thomas, M.E., Calder, E.S., Ebmeier, S.K., Telford, A., Murphy, W., Neuberg, J., 2019. Presentation and analysis of a worldwide database for lava dome collapse events: the global archive of dome instabilities (GLADIS). Bull. Volcanol. 81 (3). https://doi.org/10.1007/s00445-019-1276-y.

Harris, A.J., Rowland, S.K., 2015. Lava flows and rheology. In: The Encyclopedia of Volcanoes. Academic Press, pp. 321–342.

Heap, M.J., Russell, J.K., Kennedy, L.A., 2016. Mechanical behaviour of dacite from Mount St. Helens (USA): a link between porosity and lava dome extrusion mechanism (dome or spine)? J. Volcanol. Geotherm. Res. 328, 159–177. https://doi.org/10.1016/j.jvolgeores.2016.10.015.

Holohan, E.P., Poppe, S., Delcamp, A., Byrne, P.K., Walter, T.R., van Wyk de Vries, B., Kervyn, M., 2023. Transition from volcano-sagging to volcano-spreading. Earth Planet. Sci. Lett. 604, 118012. https://doi.org/10.1016/j.epsl.2023.118012.

Hubbert, M.K., 1937. Theory of scale models as applied to the study of geologic structures. GSA Bull. 48 (10), 1459–1520. https://doi.org/10.1130/gsab-48-1459.

Huppert, H.E., Shepherd, J.B., Sigurdsson, R.H., Sparks, S.J., 1982. On lava dome growth, with application to the 1979 lava extrusion of the Soufriere of St. Vincent. J. Volcanol. Geotherm. Res. 14 (3–4), 199–222.

Husain, T., Elsworth, D., Voight, B., Mattioli, G., Jansma, P., 2018. Influence of conduit flow mechanics on magma rheology and the growth style of lava domes. Geophys. J. Int. 213 (3), 1768–1784. https://doi.org/10.1093/gji/ggy073.

Husain, T., Elsworth, D., Voight, B., Mattioli, G., Jansma, P., 2019. Morphologic variation of an evolving dome controlled by the extrusion of finite yield strength magma. J. Volcanol. Geotherm. Res. 370, 51–64. https://doi.org/10.1016/j.jvolgeores.2019.01.010.

Hutchison, W., Varley, N., Pyle, D.M., Mather, T.A., Stevenson, J.A., 2013. Airborne thermal remote sensing of the Volcan de Colima (Mexico) lava dome from 2007 to 2010. Remote Sens. Volcanoes Volcan. Process. Integrat. Observ. Model. 380 (1), 203–228. https://doi.org/10.1144/Sp380.8.

Iverson, R.M., 1990. Lava domes modeled as brittle shells that enclose pressurized magma, with application to mount St. Helens, Lava Flows and Domes. In: IAVCEI Proceedings in Volcanology, pp. 47–69. https://doi.org/10.1007/978-3-642-74379-5_3.

Iverson, R.M., 2008. Dynamics of Seismogenic Volcanic Extrusion Resisted by a Solid Surface Plug, Mount St. Helens, 2004-2005. 1750-21, Reston, VA. https://doi.org/10.3133/pp175021.

Kaneko, T., Wooster, M.J., Nakada, S., 2002. Exogenous and endogenous growth of the Unzen lava dome examined by satellite infrared image analysis. J. Volcanol. Geotherm. Res. 116 (1), 151–160. https://doi.org/10.1016/S0377-0273(02)00216-0.

Kavanagh, J.L., Engwell, S.L., Martin, S.A., 2018. A review of laboratory and numerical modelling in volcanology. Solid Earth 9 (2), 531–571. https://doi.org/10.5194/se-9-531-2018.

Lacroix, A., 1904. La Montagne Pelee et Ses Eruptions. Masson Paris, Paris.

Lavallée, Y., Hess, K.-U., Cordonnier, B., Dingwell, D.B., 2007. Non-Newtonian rheological law for highly crystalline dome lavas. Geology 35 (9), 843. https://doi.org/10.1130/g23594a.1.

Luhr, J.F., Carmichael, I.S., 1980. The Colima volcanic complex, Mexico: I. post-caldera andesites from Volcán Colima. Contrib. Mineral. Petrol. 71, 343–372.

Melnik, O., Sparks, R.S.J., 2005. Controls on conduit magma flow dynamics during lava dome building eruptions. J. Geophys. Res. Solid Earth 110 (B2). https://doi.org/10.1029/2004jb003183.

Mériaux, C.A., May, D.A., Jaupart, C., 2022. The impact of vent geometry on the growth of lava domes. Geophys. J. Int. 229 (3), 1680–1694. https://doi.org/10.1093/gji/ggac005.

Merle, O., 2015. The scaling of experiments on volcanic systems. Front. Earth Sci. 3. https://doi.org/10.3389/feart.2015.00026.

Moussallam, Y., Peters, N., Masias, P., Apaza, F., Barnie, T., Ian Schipper, C., Curtis, A., Tamburello, G., Aiuppa, A., Bani, P., Giudice, G., Pieri, D., Davies, A.G., Oppenheimer, C., 2017. Magmatic gas percolation through the old lava dome of El Misti volcano. Bull. Volcanol. 79 (6), 46. https://doi.org/10.1007/s00445-017-1129-5.

Myers, A.J., Harnett, C.E., Holohan, E.P., Walter, T.R., Heap, M.J., 2024. The Geometric Spectrum of Lava Domes and Spines: New Perspectives from Analysis of the Morphology of Viscous Extrusions (MoVE) Global Dataset, Volcanica (In press).

Nakada, S., Motomura, Y., 1999. Petrology of the 1991-1995 eruption at Unzen: effusion pulsation and groundmass crystallization. J. Volcanol. Geotherm. Res. 89 (1–4), 173–196. https://doi.org/10.1016/S0377-0273(98)00131-0.

Nakada, S., Shimizu, H., Ohta, K., 1999. Overview of the 1990–1995 eruption at Unzen Volcano. J. Volcanol. Geotherm. Res. 89 (1–4), 1–22.

Ogburn, S.E., Loughlin, S.C., Calder, E.S., 2012. DomeHaz - Dome Forming Eruptions Database. https://theghub.org/resources/1742.

Poppe, S., Holohan, E.P., Rudolf, M., Rosenau, M., Galland, O., Delcamp, A., Kervyn, M., 2021. Mechanical properties of quartz sand and gypsum powder (plaster) mixtures: implications for laboratory model analogues for the Earth's upper crust. Tectonophysics 814, 228976. https://doi.org/10.1016/j.tecto.2021.228976.

Ryan, A.G., Friedlander, E.A., Russell, J.K., Heap, M.J., Kennedy, L.A., 2018. Hot pressing in conduit faults during lava dome extrusion: Insights from Mount St. Helens 2004–2008. Earth Planet. Sci. Lett. 482, 171–180. https://doi.org/10.1016/j.epsl.2017.11.010.

Smith, R., Sammonds, P.R., Tuffen, H., Meredith, P.G., 2011. Evolution of the mechanics of the 2004–2008 Mt. St. Helens lava dome with time and temperature. Earth Planet. Sci. Lett. 307 (1), 191–200. https://doi.org/10.1016/j.epsl.2011.04.044.

Sparks, R.S.J., Young, S.R., 2002. The Eruption of Soufriere Hills Volcano, Montserrat (1995–1999): Overview of Scientific Results.

Sparks, R.S.J., Murphy, M.D., Lejeune, A.M., Watts, R.B., Barclay, J., Young, S.R., 2000. Control on the emplacement of the andesite lava dome of the Soufriere Hills volcano, Montserrat by degassing-induced crystallization. Terra Nova 12 (1), 14–20. https://doi.org/10.1046/j.1365-3121.2000.00267.x.

Stinton, A.J., 2024. Growth and evolution of the lava dome and coulée during the 2020-21 eruption of La Soufrière, St Vincent. Geol. Soc. Lond. Spec. Publ. 539 (1), 25–39. https://doi.org/10.1144/sp539-2022-304.

Swanson, D.A., Holcomb, R.T., 1990. Regularities in growth of the Mount St. Helens Dacite Dome, 1980–1986. In: Fink, J.H. (Ed.), Lava Flows and Domes: Emplacement Mechanisms and Hazard Implications. Springer, Berlin Heidelberg, Berlin, Heidelberg, pp. 3–24. https://doi.org/10.1007/978-3-642-74379-5_1.

Tsepelev, I., Ismail-Zadeh, A., Melnik, O., 2020. Lava dome morphology inferred from numerical modelling. Geophys. J. Int. 223 (3), 1597–1609. https://doi.org/10.1093/gji/ggaa395.

Vallance, J.W., Schneider, D.J., Schilling, S.P., 2008. Growth of the 2004-2006 lava-dome complex at Mount St. Helens, Washington (no. 1750-9). US Geol. Survey 169–208.

Voight, B., Elsworth, D., 2000. Instability and collapse of hazardous gas-pressurized lava domes. Geophys. Res. Lett. 27 (1), 1–4. https://doi.org/10.1029/1999gl008389.

Wadge, G., Ryan, G., Calder, E.S., 2009. Clastic and core lava components of a silicic lava dome. Geology 37 (6), 551–554. https://doi.org/10.1130/G25747a.1.

Wadge, G., Voight, B., Sparks, R.S.J., Cole, P.D., Loughlin, S.C., Robertson, R.E.A., 2014. Chapter 1 an Overview of the Eruption of Soufrière Hills Volcano, Montserrat from 2000 to 2010, 39. The Geological Society of London, London, pp. 1–40.

Walter, T.R., Harnett, C.E., Varley, N., Bracamontes, D.V., Salzer, J., Zorn, E.U., Thomas, M.E., 2019. Imaging the 2013 explosive crater excavation and new dome formation at Volcán de Colima with TerraSAR-X, time-lapse cameras and modelling. J. Volcanol. Geotherm. Res. 369, 224–237.

Walter, T.R., Zorn, E.U., Harnett, C.E., Shevchenko, A.V., Belousov, A., Belousova, M., Vassileva, M.S., 2022. Influence of conduit and topography complexity on spine extrusion at Shiveluch volcano, Kamchatka. Commun. Earth Environ. 3 (1), 169. https://doi.org/10.1038/s43247-022-00491-w.

Watts, R.B., Herd, R.A., Sparks, R.S.J., Young, S.R., 2002. Growth patterns and emplacement of the andesitic lava dome at Soufrière Hills Volcano, Montserrat. Geol. Soc. Lond. Mem. 21 (1), 115–152. https://doi.org/10.1144/gsl.Mem.2002.021.01.06.

Závada, P., Dědeček, P., Lexa, J., Keller, G.R., 2015. Devils Tower (Wyoming, USA): A lava coulée emplaced into a maar-diatreme volcano? Geosphere 11 (2), 354–375.

Zeinalova, N., Ismail-Zadeh, A., Melnik, O., Tsepelev, I., Zobin, V., 2021. Lava dome morphology and viscosity inferred from data-driven numerical modeling of dome growth at Volcan de Colima, Mexico during 2007-2009. Front. Earth Sci. 9 (1092), 735914. https://doi.org/10.3389/feart.2021.735914.

Zorn, E.U., Le Corvec, N., Varley, N.R., Salzer, J.T., Walter, T.R., Navarro-Ochoa, C., Vargas-Bracamontes, D.M., Thiele, S.T., Mendoza, R.A., 2019. Load stress Controls on Directional Lava Dome Growth at Volcan de Colima, Mexico. Front. Earth Sci. 7, 84. https://doi.org/10.3389/feart.2019.00084.

Zorn, E.U., Walter, T.R., Heap, M.J., Kueppers, U., 2020. Insights into lava dome and spine extrusion using analogue sandbox experiments. Earth Planet. Sci. Lett. 551. https://doi.org/10.1016/j.epsl.2020.116571.